Polar cap potential saturation, dayside reconnection, and changes to the magnetosphere

Joseph E. Borovsky,[1] Benoit Lavraud,[1,2] and Maria M. Kuznetsova[3]

Received 7 January 2009; accepted 21 January 2009; published 31 March 2009.

[1] Global MHD simulations of the Earth's magnetosphere using the Block-Adaptive-Tree Solarwind Roe Upwind Scheme code at the Community Coordinated Modeling Center are run with a high-resolution dayside magnetopause and variable-resolution near-Earth regions to study the phenomena of polar cap saturation. In the simulations a resistive spot is maintained on the moving magnetopause to ensure that the correct dayside reconnection rate is obtained. The solar wind parameters are held fixed, and the ionospheric Pedersen conductivity is varied. Strong reduction of the cross–polar cap potential is observed, with modest increases in the cross–polar cap current, and no changes in the local and global reconnection rates. Changes in the magnetosphere associated with the saturation of the polar cap are explored: these include a weakening of the dayside magnetic field strength, an equatorward shift of the cusps, a flattening in Z of the closed field line region of the dayside magnetosphere, and a taillike stretching of the dipole field lines at the terminator. Measurements of the currents and voltages of the polar cap indicate that the solar wind acts like a current-limited voltage generator. A simple circuit model is analyzed using measurements from the MHD simulations, and physically reasonable values for the circuit elements are obtained. Nine models for polar cap saturation are assessed against the findings of the present study.

Citation: Borovsky, J. E., B. Lavraud, and M. M. Kuznetsova (2009), Polar cap potential saturation, dayside reconnection, and changes to the magnetosphere, *J. Geophys. Res.*, *114*, A03224, doi:10.1029/2009JA014058.

1. Introduction

[2] At times, the cross–polar cap potential "saturates." What saturation means is that the cross–polar cap potential in the ionosphere is less than expected for a given strength of the solar wind driver [e.g., *Wygant et al.*, 1983; *Reiff and Luhmann*, 1986; *Weimer et al.*, 1990].

[3] Statistically, saturation of the polar cap tends to happen (1) during stormtimes, (2) during solar maximum, and (3) during low–Mach number solar wind [*Borovsky and Denton*, 2006a; *Lavraud and Borovsky*, 2008]. Saturation happens often when a magnetic cloud passes the Earth.

[4] The occurrence of polar cap saturation for CME-driven geomagnetic storms is one of several differences between CIR-driven and CME-driven storms [*Borovsky and Denton*, 2006a]. Polar cap saturation can be an important aspect of CME-driven storms. The resulting reduction in the polar cap voltage raises issues about reduced convection in the stormtime magnetosphere, with convection driving stormtime phenomena such as the aurora and the ring current and with convection perhaps being important for the evolution of the radiation belts.

[5] There are several polar cap saturation models in the literature. (For reviews see *Siscoe et al.* [2004], *Shepherd* [2007], or *Lavraud and Borovsky* [2008].) A polar cap saturation model attempts to explain why the polar cap voltage is reduced from its expected value. The models can be separated into "reconnection" models and "postreconnection" models: reconnection models explain the reduced potential as being caused by a reduction in the dayside reconnection rate and postreconnection models explain the reduced potential with processes happening on newly reconnected field lines. Polar cap saturation models will be discussed and assessed in Appendix A.

[6] Measurements of the cross–polar cap potential $\Delta\varphi_{pc}$ in the ionosphere have been fit with the functional form [cf. *Ober et al.*, 2003; *Hairston et al.*, 2005]

$$\Delta\varphi_{pc} = \Delta\varphi_o/(1 + Q) \tag{1}$$

where $\Delta\varphi_o$ is the cross–polar cap potential expected for the amount of solar wind driving and Q is a saturation parameter. Using the formulation of *Siscoe et al.* [2004], Q can be written

$$Q = v_A \Sigma_P/806 \tag{2}$$

(see *Borovsky and Denton* [2006a] for a derivation), where v_A (in units of km s^{-1}) is the Alfven speed of the solar wind plasma upstream of the bow shock and Σ_P (in units of mho)

[1]Los Alamos National Laboratory, Los Alamos, New Mexico, USA.
[2]Now at Centre d'Etude Spatiale des Rayonnements, UMR5187, CNRS, Toulouse, France.
[3]NASA Goddard Space Flight Center, Greenbelt, Maryland, USA.

Copyright 2009 by the American Geophysical Union.
0148-0227/09/2009JA014058

is the height-integrated Pedersen conductivity of the ionosphere. The factor of 1/806 in expression (2) contains a numerical factor that was evaluated by *Siscoe et al.* from a global MHD simulation of the magnetosphere. Using the theoretical formulation of *Kivelson and Ridley* [2008] [see also *Ridley*, 2007], Q can be obtained by equating the cross–polar cap current to the Alfven-conductance-limited field-aligned current of the solar wind, which yields

$$Q = v_A \Sigma_P / 795. \tag{3}$$

[7] When the Alfven speed v_A of the solar wind plasma is high and/or when the conductivity Σ_P of the ionosphere is high, the polar cap saturation factor Q tends to be large and the polar cap voltage as given by expression (1) is reduced. The Alfven speed of the solar wind plasma is $v_A = B/(4\pi n m_i)^{1/2}$. The Alfven speed of the solar wind is high when the magnetic field strength B is large and the plasma number density n is small; this typically occurs for magnetic clouds [e.g., *Gosling et al.*, 1987; *Borovsky and Denton*, 2006a; *Lavraud and Borovsky*, 2008]. The Pedersen conductivity of the ionosphere is driven by the UV flux of the sun; that flux is high during solar maximum [cf. *Floyd et al.*, 2005].

[8] In this paper the phenomenology associated with polar cap saturation is explored using high-resolution 3-D MHD simulations of the solar wind–driven magnetosphere. Special care is taken to ensure that the simulation code obtains the correct dayside reconnection rate. In the MHD simulations discussed in this paper, only the polar cap Pedersen conductivity Σ_P and the grid resolution of the computer code are varied; the solar wind parameters are kept fixed. Several effects associated with the saturation phenomena are investigated.

[9] The simulations provide information useful for assessing the various models of polar cap saturation and they provide information and insight into the mechanics of how the solar wind–driven magnetosphere operates. The reader is cautioned, however, that global MHD codes may do things incorrectly and results and insights need to be checked with actual measurements.

[10] This manuscript is organized as follows. In section 2 the numerical simulation method used to explore polar cap saturation is described. In section 3 the cross–polar cap potential and the polar cap current in the simulations are analyzed. In section 4 the local reconnection rate at the magnetopause and the global dayside reconnection rate are analyzed. Changes to the magnetosphere associated with polar cap saturation are explored in section 5. Section 6 contains discussions about (1) the constancy of the dayside reconnection rate, (2) how the polar cap saturation in the simulations acts like a current-limited voltage generator, and (3) a circuit analysis of the polar cap saturation behavior seen in the simulations. The findings of this study are summarized in section 7. In Appendix A models of polar cap saturation in the literature are assessed against the findings of this paper.

2. MHD Simulations

[11] Simulations of the solar wind–driven magnetosphere-ionosphere system are run at the Community Coordinated Modeling Center (CCMC) [*Bellaire*, 2004] at NASA/Goddard Space Flight Center using the Block-Adaptive-Tree Solarwind Roe Upwind Scheme (BATSRUS) 3-D MHD code [*Powell et al.*, 1999; *De Zeeuw et al.*, 2000; *Gombosi et al.*, 2000; *Ridley et al.*, 2004; A. J. Ridley and G. Toth, unpublished data, 2008]. The code is used in a unique manner to (1) obtain a physically correct dayside reconnection rate and (2) to have accurate, high-resolution mapping of currents between the magnetosphere and the polar cap of the ionosphere.

[12] As in the paper by *Borovsky et al.* [2008], a $\Delta X = \Delta Y = \Delta Z = 1/16\ R_E$ spatial resolution numerical grid is used in the region of the dayside magnetopause in the BATSRUS code. The grid resolution for the near-Earth region is taken to be 1/4 R_E (low), 1/8 R_E (medium), or 1/16 R_E (high) in various runs to discern the effects of better and better resolution for mapping currents into and out of the ionosphere. These three resolutions are depicted in Figures 1 (top), 1 (middle), and 1 (bottom), where three cuts through the computational grid in the X = 0 plane are shown. With the high-resolution near-Earth region, the simulations use a total of 21.5 million grid points.

[13] The inner boundary of the simulation domain is at $r = 2.5\ R_E$. Near-Earth boundary conditions are determined by a two-dimensional electrostatic solver [*Goodman*, 1995] that uses the field-aligned currents from the global magnetosphere to solve for the ionospheric potential and delivers convection velocity back to the inner boundary of the MHD simulation. The currents are mapped along the dipole field lines from $r = 3R_E$ near the inner boundary of the MHD domain down to the ionosphere [*Ridley et al.*, 2004]. For the present simulations, constant Pedersen conductivity and zero Hall conductivity is used.

[14] As in the paper by *Borovsky et al.* [2008], a localized region ("spot") of high resistivity is added to the nose of the magnetosphere to ensure that the reconnection is in the Petschek (fast) mode and that the reconnection rate calculated by MHD at the dayside magnetopause is correct. As explained in the appendix of *Borovsky et al.* [2008], if the resistivity of the spot is strong enough to allow the magnetic field to fully diffuse out of the plasma as it flows across the spot, then the reconnection rate is independent of the properties of the spot [*Birn and Hesse*, 2001, 2007; *Birn et al.*, 2008]. The resistivity of the spot is chosen to be about an order of magnitude higher than the numerical resistivity observed in the code without the resistivity spot. The spot is centered on the B_z reversal at the magnetopause (northward in the magnetosphere and southward in the magnetosheath) and the spot location is updated every 10 time steps in the simulation as the magnetopause location moves. The X location of the B_z reversal is denoted as $X_o(Y, Z)$ and X_o is updated separately for every value of Y and Z. The spot is narrow in the X direction, longer in the Z direction, and even longer in the Y direction. The resistivity of the spot has a hyperbolic-secant profile as a function of X, Y, and Z, which is

$$\eta = 1.26 \times 10^5\ \text{ohm} - \text{m}\,\text{sech}((X - X_o)/L_x)\,\text{sech}(Y/L_y)\,\text{sech}(Z/L_z), \tag{4}$$

where $L_x = 1/8\ R_E$, $L_y = 4\ R_E$, and $L_z = 1\ R_E$. Note that the peak resistivity of 1.26×10^5 ohm-m corresponds to a peak

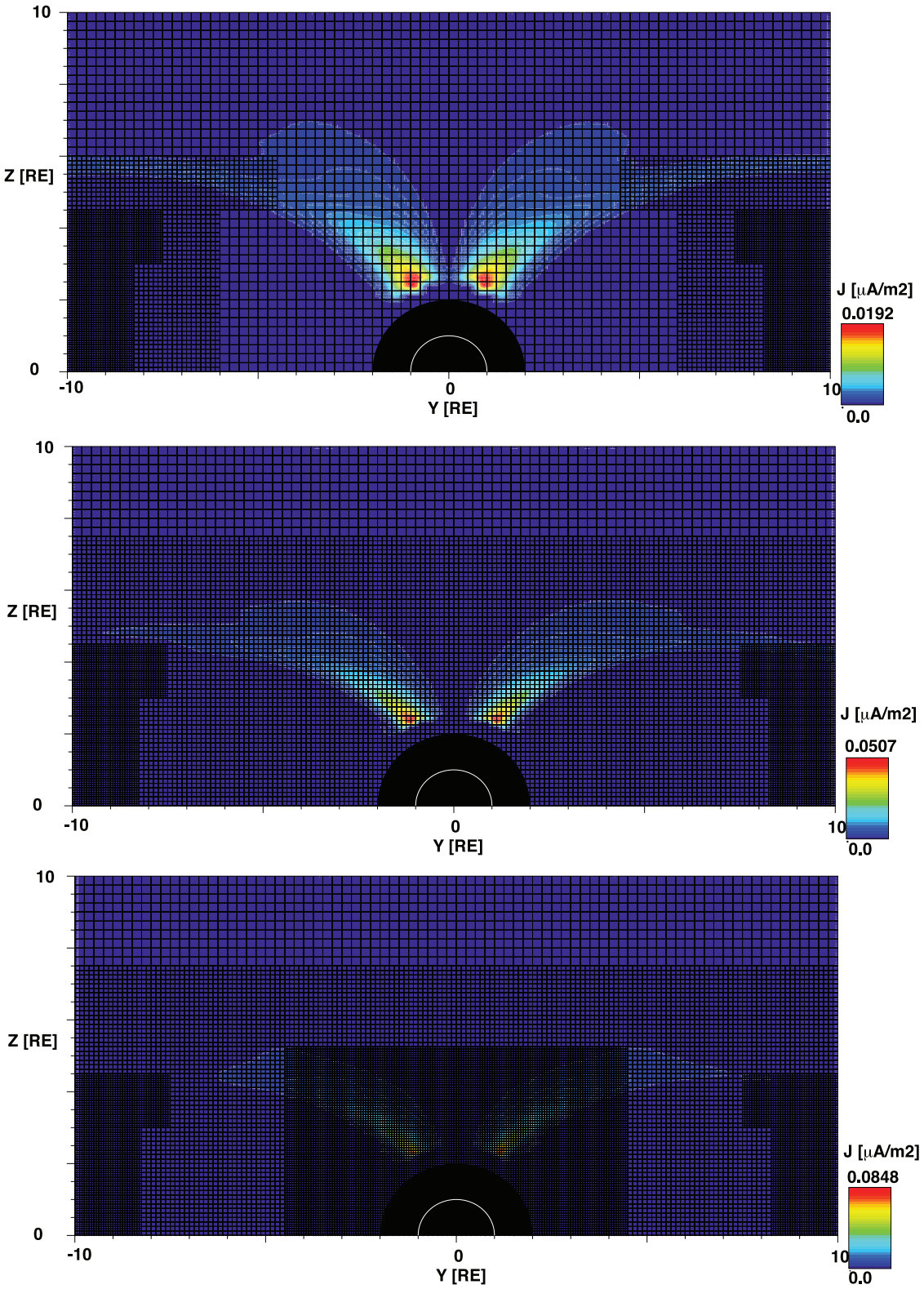

Figure 1. Depictions of the grids used in the (top) "low-resolution" (1/4 R_E), (middle) "medium-resolution" (1/8 R_E), and (bottom) "high-resolution" (1/16 R_E) simulations. The grid resolution refers to the near-Earth region (and over the polar cap). Shown are cuts in the X = 0 (dawn-dusk terminator) plane. Note the 1/16 R_E resolution of the dayside-magnetopause region which can be seen extending through the terminator plane. The total current density in μA m^{-2} in the X = 0 plane is denoted by the colors; note as the resolution increases, the polar cap current is narrower.

Table 1. Parameters of the Simulations Employed in This Polar Cap Saturation Study

Quantity	Symbol	Range
Dipole tilt	θ	none
Solar wind radial velocity	v_x	-300 km s^{-1}
Solar wind east–west velocity	v_y	0
Solar wind north–south velocity	v_z	0
Solar wind number density	n	2 cm^{-3}
Solar wind radial magnetic field strength	B_x	0
Solar wind east–west magnetic field strength	B_y	0
Solar wind north–south magnetic field strength	B_z	-10 nT
Solar wind temperature	T	50,000 °K
Solar wind ram pressure	ρv^2	0.3 nPa
Solar wind electric field	E_y	3 mV m^{-1}
Alfven speed in solar wind	v_A	156 km s^{-1}
Acoustic speed in solar wind	C_s	20.3 km s^{-1}
Magnetosonic speed in solar wind	C_{ms}	157 km s^{-1}
Alfven Mach number of solar wind	M_A	1.9
Magnetosonic Mach number of solar wind	M_{ms}	1.9
Height-integrated Pedersen conductivity of ionospheres	Σ_P	5–20 mho
Height-integrated Hall conductivity of ionospheres	Σ_H	0
Polar cap saturation parameter	Q	0.97–3.9
Maximum resistivity of spot	η	1.26×10^5 Ω–m
Simulation inner boundary	r_{min}	2.5 R_E
Simulation-box outer boundary	X_{max}	33 R_E
Simulation-box outer boundary	X_{min}	-255 R_E
Simulation-box outer boundary	Y_{max}	48 R_E
Simulation-box outer boundary	Y_{min}	-48 R_E
Simulation-box outer boundary	Z_{max}	48 R_E
Simulation-box outer boundary	Z_{min}	-48 R_E

magnetic diffusivity of $\eta/\mu_o = 1 \times 10^{11}$ m^2 s^{-1}. The motivation for the spot is from the results of the GEM challenge [*Birn et al.*, 2001] wherein it was shown that resistive MHD simulations can yield the correct reconnection rate if a spot of localized high resistivity is placed on the reconnection site [see also *Ugai and Tsuda*, 1977; *Yan et al.*, 1992; *Birn and Hesse*, 2001; *Borovsky and Hesse*, 2007; *Birn et al.*, 2008]. If this resistive spot technique is not used the reconnection rate is governed by errors in solving the MHD equations owing to gradients steepening to the grid scale of the numerical simulations. In essence, the resistive spot (with a thickness larger than the grid resolution) prevents gradients from steepening down to the grid scale and hence has the MHD equations (without added numerical error terms) being solved at the reconnection site. A discussion of how to select the parameters for the spot appears in the appendix of *Borovsky et al.* [2008].

[15] To reduce numerical diffusivity in the MHD simulations, the BATSRUS code is run with the second-order artificial wind solve of *Sokolov et al.* [2002].

[16] The regimes run can be discerned from Table 1. The solar wind parameters are kept fixed and the height-integrated Pedersen conductivity of the ionosphere is varied from 5 mho to 20 mho and the resolution of the simulation in the near-Earth region and above the polar cap is varied. No corotation is added and there is no dipole tilt. Note that the Alfven Mach number of the solar wind is low (M_A = 1.9) so that polar cap saturation is acting even at modest values of the ionospheric conductivity.

[17] As can be assessed from Table 1, polar cap saturation will be explored when the magnetosphere is modestly driven (v = 300 km s^{-1} and $B_z = -10$ nT). Some of the global MHD simulations in the literature have also explored polar cap saturation in this modestly driven regime [e.g., *Fedder and Lyon*, 1987; *Siscoe et al.*, 2002a; *Ridley et al.*, 2004]. Other simulations have explored polar cap saturation with very strong driving [e.g., *Raeder et al.*, 2001; *Merkin et al.*, 2005b; *Raeder and Lu*, 2005; *Ridley et al.*, 2006] or have varied their solar wind parameters into the very strongly driven regime [e.g., *Siscoe et al.*, 2002b; *Merkine et al.*, 2003; *Merkin et al.*, 2005a; *Ridley*, 2007; *Lavraud and Borovsky*, 2008].

3. Polar Cap Saturation

[18] In the BATSRUS MHD simulations, when the ionospheric Pedersen conductivity is varied to produce a variation in the polar cap saturation factor Q, the cross–polar cap potential in the ionosphere varies approximately as predicted by the polar cap saturation formula (expression (1)). This is demonstrated in Figure 2 with a simulation with a low-resolution near-Earth region (but always with a high-resolution dayside magnetopause). With the solar wind parameters fixed, the Pedersen conductivity Σ_P of the ionosphere is slowly changed from 5 mho to 20 mho (Figure 2 (bottom)) and the cross–polar cap potential $\Delta\varphi_{pc}$ in the ionosphere is measured (Figure 2 (top)). As can be seen in Figures 2 (top) and 2 (middle), when the Pedersen conductivity increases, the polar cap potential decreases. According to expression (1), the potential $\Delta\varphi_{pc}$ of the polar cap should vary as $\Delta\varphi_{pc} = \Delta\varphi_o/(1 + Q)$, where $Q = v_A\,\Sigma_P/806$ (where Σ_P is in mho and v_A is in km s^{-1}) is the polar cap saturation factor and $\Delta\varphi_o$ is the polar cap potential in the absence of any ionospheric saturation effects. The polar cap saturation factor Q is plotted in Figure 2 (bottom), as is the factor $(1 + Q)^{-1}$. As can be seen by comparing the curves in Figures 2 (top) and 2 (bottom), the measured cross–polar cap potential $\Delta\varphi_{pc}$ varies approximately as $(1 + Q)^{-1}$ in the simulations. (See also the simulations of *Siscoe et al.* [2002a] and *Merkin et al.* [2005b] for this $(1 + Q)^{-1}$ behavior.) A fit to the measured polar cap potential of the form $\Delta\varphi_o/(1 + Q)$ yields $\Delta\varphi_o$ = 121 kV for the simulation of Figure 2.

[19] In Figure 3 the cross–polar cap potential $\Delta\varphi_{pc}$ measured in the simulations is plotted as a function of time as the grid resolution of the near-Earth region is switched. The solid points are from a simulation with Σ_P = 5 mho and the hollow points are from a simulation with Σ_P = 20 mho. At t = 20 min the resolution changed from 1/4 R_E (low; see Figure 1 (top)) to 1/8 R_E (medium; Figure 1 (middle)) and at t = 70 min the resolution changed from 1/8 R_E (medium) to 1/16 R_E (high; Figure 1 (bottom)). These grid resolutions are indicated by the horizontal arrows in Figure 3. As can be seen, the polar cap potentials $\Delta\varphi_{pc}$ in the simulations increase when a higher-resolution near-Earth region is utilized. This increase in the ionospheric potentials with an increase in the resolution of the near-Earth region has been systematically studied with the BATSRUS code by A. J. Ridley and G. Toth (unpublished data, 2008). They found that an increase in the near-Earth grid resolution brings the ionospheric potential closer to the true value. Their conclusion is that at 1/16 R_E resolution (the highest they explored)

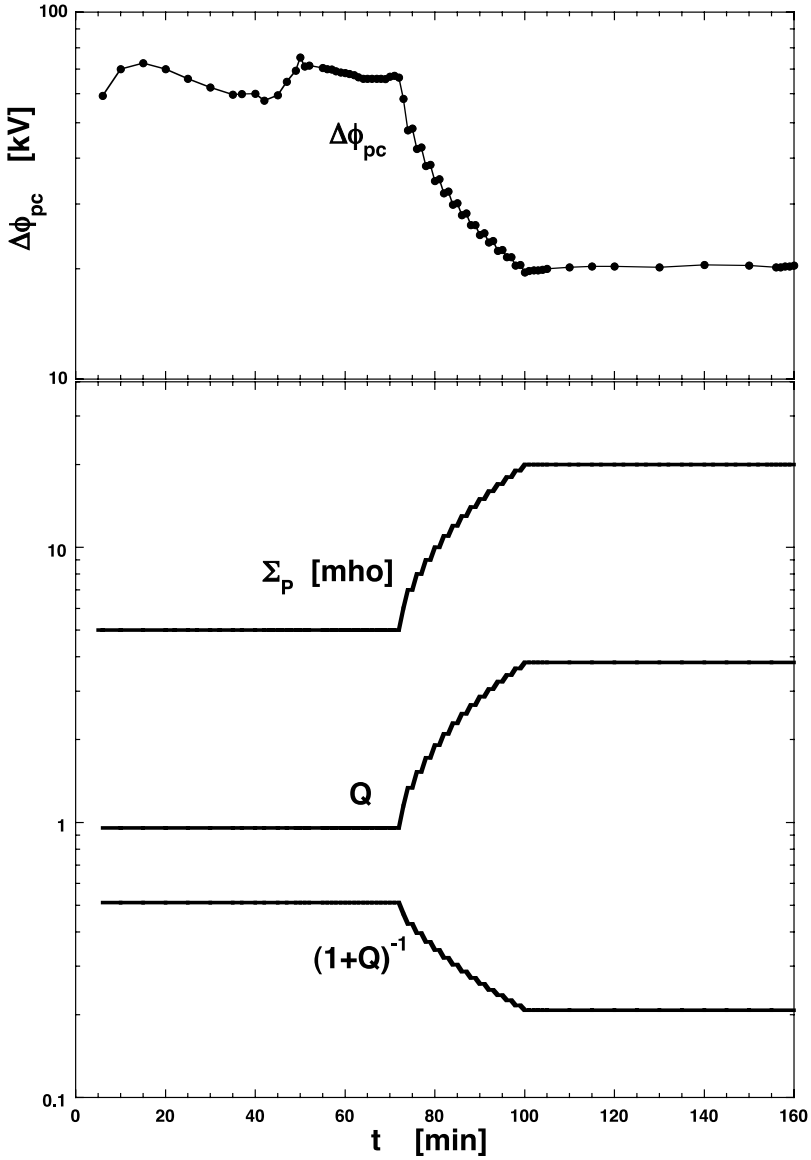

Figure 2. From simulations with a low-resolution near-Earth region, several quantities are plotted as a function of time. (bottom) For steady solar wind parameters, the Pedersen conductivity Σ_P of the ionosphere is ramped up with time. This changes the value of Q and the value of $(1 + Q)^{-1}$ (Figure 2 (bottom)). (top) In reaction to the increase in SP, the cross–polar cap potential $\Delta\varphi_{pc}$ reduces. The solar wind parameters are fixed at v = 300 km s^{-1}, $B_z = -10$ nT, and n = 2 cm^{-3}.

the polar cap potential had not yet reached its true value but that it was approaching grid convergence. From Figure 3 the polar cap potentials $\Delta\varphi_{pc}$ for the various resolution values are averaged and collected into Table 2.

[20] Using the $\Delta\varphi_{pc}$ values collected in Table 2 for Σ_P = 5 mho and Σ_P = 20 mho, the ratio of $\Delta\varphi_{pc}$ at 5 mho to $\Delta\varphi_{pc}$ at 20 mho is calculated and entered into Table 3 for the three values of the near-Earth region (and over the polar caps) grid resolution. For a $\Delta\varphi_{\perp}(1 + Q)^{-1}$ behavior with Σ_P = 5 mho (Q = 0.97) and Σ_P = 20 mho (Q = 3.9), the predicted ratio of polar cap potentials $\Delta\varphi_{pc}$(5 mho)/$\Delta\varphi_{pc}$(20 mho) is (1 + 3.9)/(1 + 0.97) = 2.5: this predicted ratio is entered as the second column of Table 3. The fractional difference between the measured ratio of $\Delta\varphi_{pc}(5)/\Delta\varphi_{pc}(20)$ and the prediction is entered into the third column of Table 3. As can be seen in Table 3, the prediction of a $(1 + Q)^{-1}$ behavior holds, particularly for a medium- or high-resolution near-Earth region.

[21] With a reduction in the cross–polar cap potential, one should expect a reduction in the strength of the electric field above the polar cap. In Figure 4 (top) the perpendicular (to $\underline{B}$) component of the electric field $E_{\perp}$ is plotted as a function of Z over the northern polar cap along the line segment from (X, Y, Z) = (0, 0, 3) to (X, Y, Z) = (0, 0, 14) for two high-resolution simulations: one with Σ_P = 5 mho and one with Σ_P = 20 mho. As can be seen, $E_{\perp}$ is reduced in the Σ_P = 20 mho case from its values in the Σ_P = 5 mho case. The ratio $E_{\perp}$(5 mho)/$E_{\perp}$(20 mho) of the two $E_{\perp}$ curves is plotted as the dashed curve in Figure 4 (top). A reduction by $(1 + Q)^{-1}$ for Q = 0.97 going to Q = 3.9 (see Table 1)

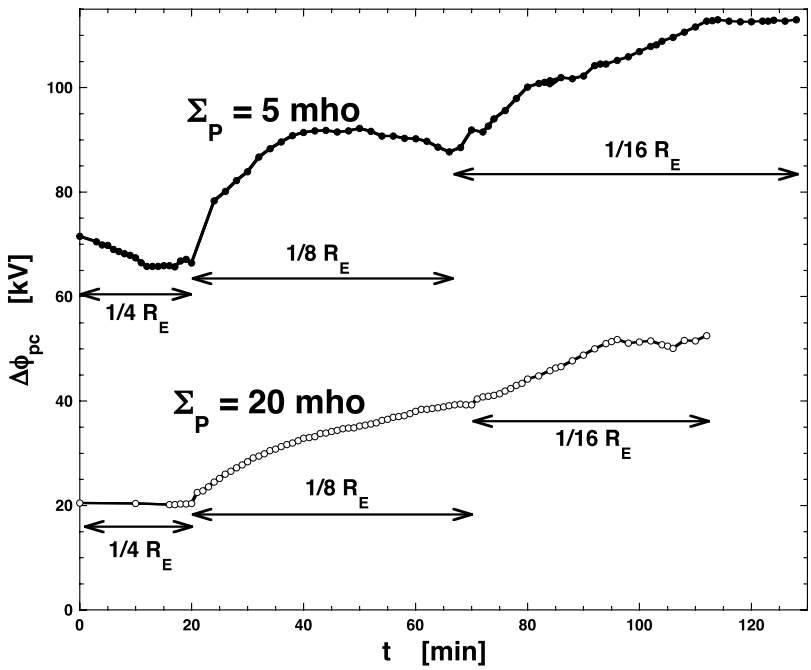

Figure 3. The polar cap potential $\Delta\varphi_{pc}$ in the ionosphere is plotted as a function of time for two simulations: one with $\Sigma_P = 5$ mho (solid points) and one with $\Sigma_P = 20$ mho (hollow points). As indicated in Figure 3, the resolution of the near-Earth region in the simulations changes with time from 1/4 R_E (low) to 1/8 R_E (medium) to 1/16 R_E (high). The solar wind parameters are fixed at $v = 300$ km s^{-1}, $B_z = -10$ nT, and $n = 2$ cm^{-3}.

predicts a ratio of 2.5: a ratio 2.25 is observed over the polar cap, which is the ratio of $\Delta\varphi_{pc}(5)/\Delta\varphi_{pc}(20)$ for the high-resolution simulations (see Table 3).

[22] In Figure 4 (bottom) the perpendicular (to $\underline{B}$) component of the plasma flow velocity $v_\perp$ is plotted as a function of Z over the northern polar cap along the line segment from (X, Y, Z) = (0, 0, 3) to (X, Y, Z) = (0, 0, 14) for the same two high-resolution simulations as in Figure 4 (top). The plasma flow velocity $v_\perp$ is also the field line convection velocity. As can be seen, $v_\perp$ is reduced in the $\Sigma_P = 20$ mho case from its values in the $\Sigma_P = 5$ mho case. The ratio $v_\perp(5\text{ mho})/v_\perp(20\text{ mho})$ of the two $v_\perp$ curves is plotted as the dashed curve in Figure 4 (top). As was the case for $E_\perp$ in Figure 4 (top), a ratio 2.25 is observed over the polar cap, which is the ratio of $\Delta\varphi_{pc}(5)/\Delta\varphi_{pc}(20)$ for the high-resolution simulations (see Table 3).

[23] In Figures 5 and 6, the currents flowing between the ionosphere and magnetosphere are explored. In Figure 5 (top) the vertical current density into (blue) and out of (red) the northern ionosphere is shown at a time when the Pedersen conductivity is $\Sigma_P = 20$ mho. Noon is at the top. As can be seen the major current system has current flowing into the ionosphere on the dawn side and out on the dusk side. In Figure 5 (middle) the magnitude |J| of the height-integrated current density flowing in the ionosphere is shown in color, with vectors added showing the direction

Table 2. Key Parameters[a]

Quantity	Resolution	$\Sigma_P = 5$ mho	$\Sigma_P = 20$ mho
	Measured Quantities		
Q	all	0.97	3.9
$\Delta\varphi_{pc}$	low	68.1 kV	20.3 kV
	medium	90.7 kV	37.7 kV
	high	113 kV	51.0 kV
I_{total}	low	1.13 MA	1.31 MA
	medium	1.50 MA	2.48 MA
	high	1.83 MA	2.84 MA
$\Delta\varphi_{mag}$	low	227 kV	156 kV
	medium	161 kV	156 kV
	high	165 kV	148 kV
R	low	1.16 mV m^{-1}	1.12 mV m^{-1}
	medium	1.15 mV m^{-1}	1.12 mV m^{-1}
	high	1.12 mV m^{-1}	1.13 mV m^{-1}
	Calculated Ratios		
$I_{total}/\Sigma_P\Delta\varphi_{pc}$	low	3.33	3.20
	medium	3.27	3.34
	high	3.25	2.78
$\Delta\varphi_{mag}/\Delta\varphi_{pc}$	low	3.33	7.68
	medium	1.77	4.14
	high	1.46	2.90

[a]Parameters were measured in the simulations at $\Sigma_P = 5$ mho and $\Sigma_P = 20$ mho at three different resolutions for the near-Earth region. Quantities are 20-min averages.

Table 3. Measured Ratio of Voltages for the $\Sigma_P = 5$ mho and $\Sigma_P = 20$ mho Simulations Compared With the Predicted Ratio of Voltages[a]

Inner Magnetosphere Grid	$\Delta\varphi_{pc}(5\text{ mho})/\Delta\varphi_{pc}(20\text{ mho})$	$(1 + Q_{20})/(1 + Q_5)$	Difference (%)
Low resolution	3.35	2.5	+34
Medium resolution	2.41	2.5	−4
High resolution	2.22	2.5	−11

[a]Comparison was made to test whether the polar cap potential varies as $(1 + Q)-1$.

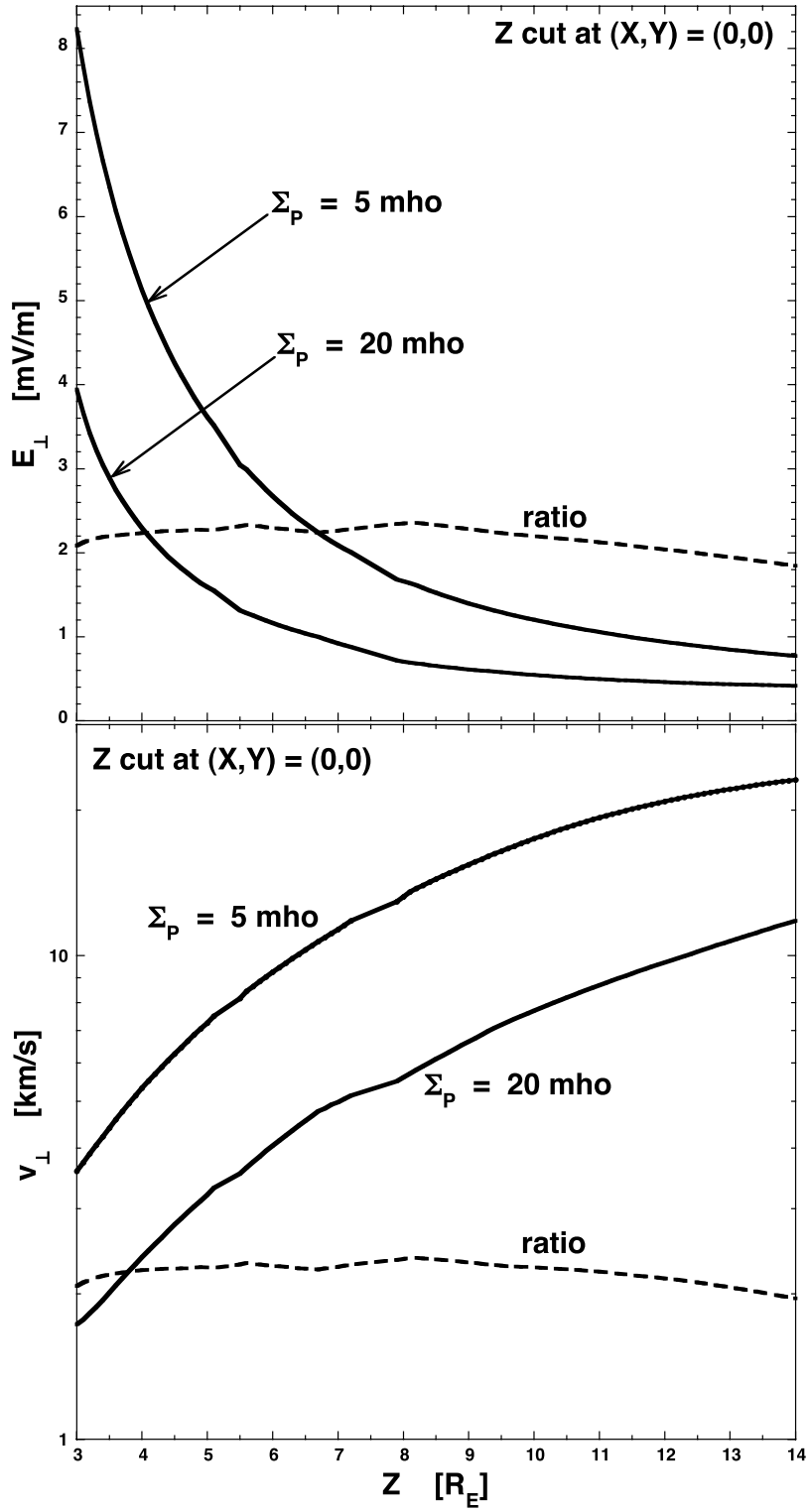

Figure 4. For two simulations with high-resolution near-Earth regions, one with Σ_P = 5 mho and one with Σ_P = 20 mho, the (top) perpendicular (to $\underline{B}$) electric field and (bottom) perpendicular (to $\underline{B}$) plasma flow velocity are plotted. The dashed curves are the ratio of the values of the two curves.

of the vector $\underline{J}$. Again, noon is at the top. As can be seen in Figure 5 (middle) there is a dawn-to-dusk Pedersen current flowing across the polar cap between the two regions where the large field-aligned currents enter and leave. This current system depicted in Figures 5 (top) and 5 (middle) has the Region-I sense [e.g., *Iijima and Potemra*, 1976]. In Figure 5 (bottom) the z component current density j_z flowing through the Z = +4 R_E plane above the northern ionosphere is shown. In Figure 5 (bottom) noon is to the right and dusk is at the top. The large Region-I current system into and out of

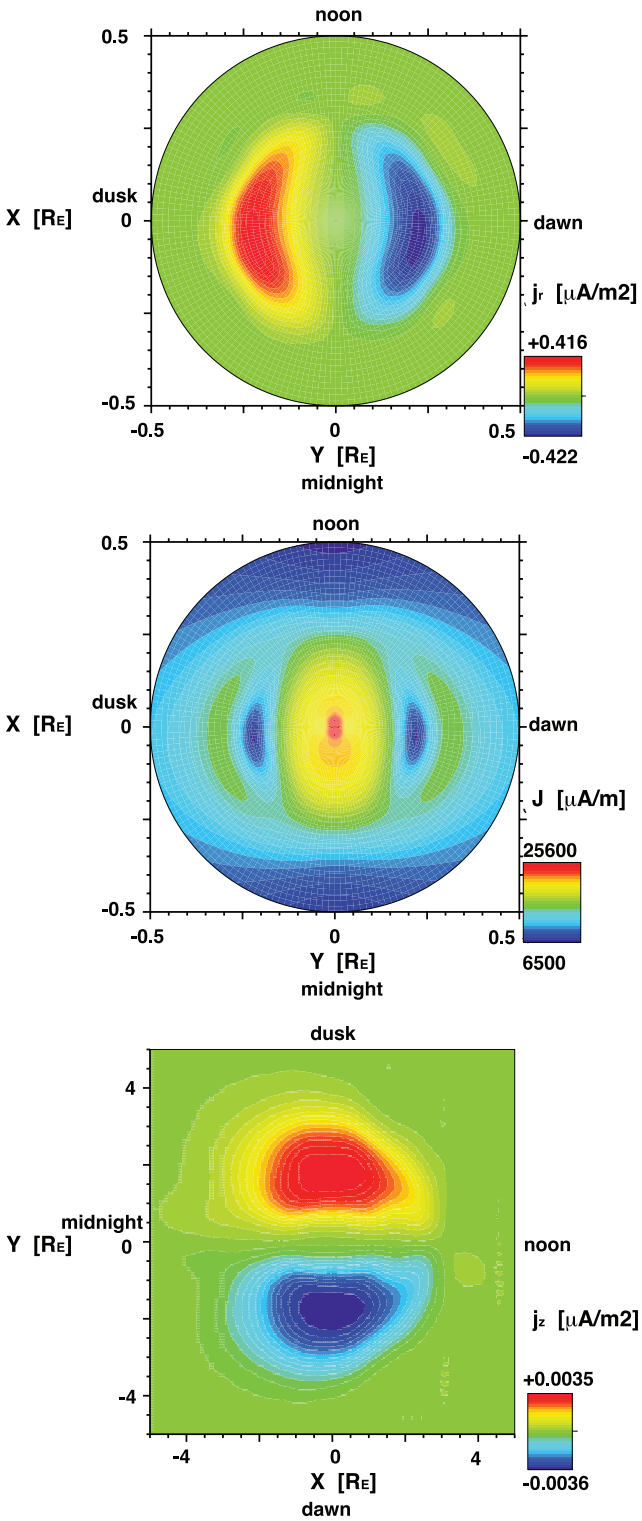

Figure 5. For a low-resolution (near-Earth region) simulation with Σ_P = 20 mho, (top) the radial current density (in μA m^{-2}) into and out of the northern ionosphere, (middle) the absolute value of the horizontal current density (in μA m^{-1}) in the ionosphere, and (bottom) the z component current density j_z passing through the Z = +4 R_E plane above the polar cap. Note that Figure 5 (bottom) is rotated by 90° from Figures 5 (top) and 5 (middle).

the ionosphere can be seen passing through this Z = +4 R_E plane.

[24] The total amount of current I_{total} flowing between the northern ionosphere and the magnetosphere is obtained by integrating the current density j_z in the MHD simulations through the Z = +4.0 R_E plane. In Figure 6 (top) the total amount of current I_{total} flowing between the ionosphere and magnetosphere is plotted as a function of time for the same two simulations that appear in Figure 3. The solid points are for the simulation with Σ_P = 5 mho and the hollow points are for the simulation with Σ_P = 20 mho. As indicated by the arrows in Figure 3, the grid resolution in the near-Earth region and over the polar caps changes with time. As can be seen in Figure 6 (top), the total current flowing I_{total} increases as the grid resolution above the polar cap increases (smaller grid steps). This increase in the current is much more pronounced for the Σ_P = 20 mho case (Q $\approx$ 4) than it is for the Σ_P = 5 mho case (Q $\approx$ 1). For the two Σ_P values and the three inner-magnetospheric resolutions values, the measurements of I_{total} plotted in Figure 6 (top) are averaged and collected into Table 2.

[25] In Figure 6 (bottom) the dimensionless geometrical factor $I_{total}/\Sigma_P\Delta\varphi_{pc}$ is plotted for the same two simulations as in Figure 6 (top). The interpretation of $I_{total}/\Sigma_P\Delta\varphi_{pc}$ is as follows [see also *Merkin et al.*, 2005b]. The horizontal Pedersen current density j flowing in the ionosphere parallel to a horizontal electric field E is given by j = σ_PE, where σ_P is the Pedersen conductivity of the plasma [e.g., *Alfven and Falthammar*, 1963; *Bostrom*, 1973]. Integrating this expression j = σ_PE vertically from the bottom of the ionosphere to the top of the ionosphere and assuming that the horizontal electric field does not vary with height, the expression becomes J = Σ_PE where J is the integral of j over height and where Σ_P is the familiar height-integrated Pedersen conductivity. The total Pedersen current I_{total} flowing in the ionosphere across the polar cap is I_{total} = JW, where W is the effective width of the current flowing. Thus, $I_{total} = \Sigma_P EW$, where E is the cross–polar cap electric field in the ionosphere. This cross–polar cap electric field is given by E = $\Delta\varphi_{pc}$/L, where $\Delta\varphi_{pc}$ is the cross–polar cap potential difference and L is the effective length of the current flowing. Thus, $I_{total} = \Sigma_P\Delta\varphi_{pc}W/L$. Hence, $I_{total}/\Sigma_P\Delta\varphi_{pc}$ = W/L is a dimensionless geometrical factor, the effective width-to-length ratio of the cross–polar cap current in the ionosphere. As can be seen in Figure 6 (bottom), values of $I_{total}/\Sigma_P\Delta\varphi_{pc}$ of about 3.5 are obtained. This indicates an effective width-to-length of the cross–polar cap current W/L of about 3.5. As can be seen in Figure 5 (middle), the width of the cross–polar cap current is considerably greater than its length.

[26] Note in Figure 6 (bottom), the factor $I_{total}/\Sigma_P\Delta\varphi_{pc}$ is approximately constant as the polar cap potential $\Delta\varphi_{pc}$ and the total current I_{total} vary substantially, and for the two values of the Pedersen conductivity Σ_P. In Figure 7 the occurrence distribution of the geometrical factor $I_{total}/\Sigma_P\Delta\varphi_{pc}$ in the simulations is shown separately for Σ_P = 5 mho (solid black points) and for Σ_P = 20 mho (hollow gray points). To construct the occurrence distributions, the values of $I_{total}/\Sigma_P\Delta\varphi_{pc}$ plotted in Figure 6 are binned. The constancy of this geometrical factor indicates that $\Delta\varphi_{pc}$ and I_{total} do not vary independently. Physically, the variation of

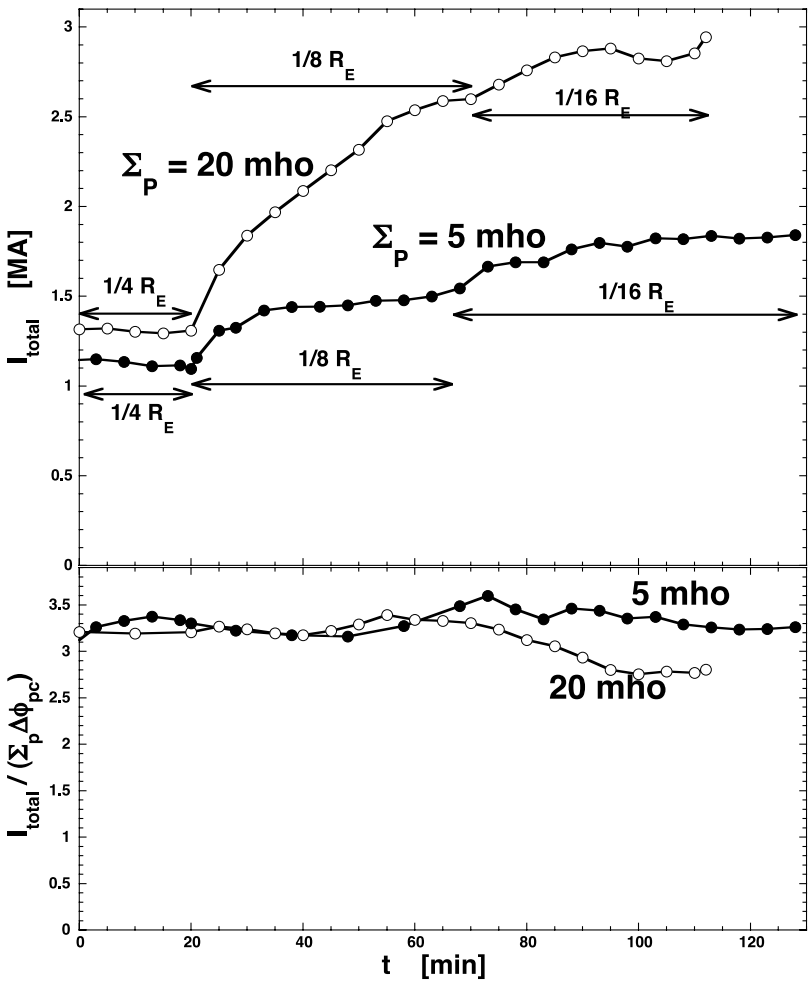

Figure 6. (top) The total amount of current I_{total} flowing between the northern ionosphere and the magnetosphere (as measured passing through the Z = +4 R_E plane) is plotted as a function of time for two simulations: one with Σ_P = 5 mho (solid points) and one with Σ_P = 20 mho (hollow points). These are the two simulations of Figure 3. As indicated in Figure 6 (top), the resolution of the near-Earth region in the simulations changes with time from 1/4 R_E (low) to 1/8 R_E (medium) to 1/16 R_E (high). (bottom) The dimensionless ratio $I_{total}/\Sigma_P\Delta\varphi_{pc}$ is plotted for the same two simulations. The solar wind parameters are fixed at v = 300 km s^{-1}, B_z = −10 nT, and n = 2 cm^{-3}.

one factor ($\Delta\varphi_{pc}$ or I_{total}) may drive the variation of the other (I_{total} or $\Delta\varphi_{pc}$).

4. Reconnection Rate at the Dayside Magnetopause

[27] As in the paper by *Borovsky et al.* [2008], the local reconnection rate near the nose of the magnetosphere is directly measured by ηj_y at the point where B_z reverses sign (the nominal magnetopause). When the BATSRUS magnetosphere was strongly driven, Borovsky *et al.* observed that a narrow plume of high-density cool plasma was pulled out of the inner magnetosphere and that the plume flowed into the dayside reconnection line at the nose, mass loading the reconnection rate on the sun-Earth line but not affecting the reconnection rate 2 R_E away from the sun-Earth line. This dense plasma mass loading dayside reconnection has been dubbed the "plasmasphere effect" [*Borovsky and Steinberg*, 2006; *Borovsky and Denton*, 2006b] owing to the mass loading of dayside reconnection by plasmaspheric drainage plumes. Because of uncontrollable plume formation in the present simulations which can depress the reconnection rate right at the nose of the magnetosphere, measurements of the local reconnection rate are made at Y = 2.5 R_E instead of at Y = 0.

[28] In Figure 8 the measured reconnection rate is plotted as a function of time for the simulation of Figure 2 with a low-resolution near-Earth region and a Pedersen conductivity that ramps up from 5 mho to 20 mho over time. Also plotted in Figure 8 is the height-integrated Pedersen conductivity Σ_P of the ionosphere and the measured cross–polar cap potential $\Delta\varphi_{pc}$ in the ionosphere. As can be seen, the dayside reconnection rate does not reduce as the polar cap potential further saturates.

[29] In Figure 9 the local reconnection rate R measured at the dayside magnetopause is plotted as a function of time for the same two simulations as in Figure 6 where the resolution of the near-Earth region changes with time. The

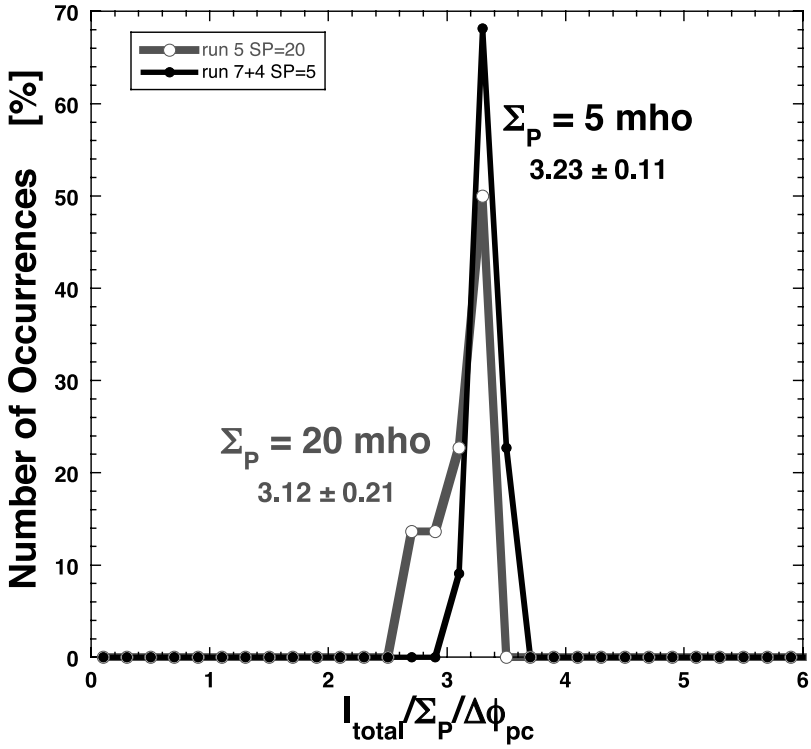

Figure 7. For the two simulations of Figure 6, the dimensionless ratio $I_{total}/\Sigma_P\Delta\varphi_{pc}$ is binned and the occurrence distribution is plotted. The solid black points pertain to the Σ_P = 5 mho simulation, and the hollow gray points pertain to the Σ_P = 20 mho simulation.

solid points are the reconnection rate in the Σ_P = 5 mho simulation and the hollow points are the reconnection rate in the Σ_P = 20 mho simulation. As can be seen, as the resolution of the near-Earth region grid changes (and the cross–polar cap potential (Figure 6 (top)) and magnetosphere-ionosphere currents (Figure 6 (middle)) change) the reconnection rate measured at the dayside magnetopause does not change. The local reconnection rate is the same in the Σ_P = 20 mho case as it is in the Σ_P = 5 mho case, regardless of the resolution of the near-Earth region.

[30] As a measure of the global reconnection rate on the dayside magnetopause, the spatial integral of E_y across the magnetosphere is calculated in the simulations. This integral has the dimension of a potential and is here denoted as $\Delta\varphi_{mag}$. This integral is a measure of the rate of convection of magnetic flux in the magnetosphere, which is a measure of the global rate of flux capture at the dayside magnetopause. Taking the integral in Y across the magnetosphere at X = −8 R_E and Z = 0 from one low-latitude boundary layer to the other, the resulting integral in units of kV is plotted as the solid points in Figure 10. The magnetospheric potential $\Delta\varphi_{mag}$ varies considerably with time in reaction to activations in the magnetotail, but no clear trend of a variation of $\Delta\varphi_{mag}$ with resolution is evident. Hence, the indications are that the global reconnection rate does not change with changes in the resolution of the near-Earth region and regions over the poles. The values of $\Delta\varphi_{mag}$ that are plotted in Figure 9 are averaged and collected into Table 2.

[31] Some of the potential $\Delta\varphi_{mag}$ across the magnetosphere is owed to the viscous interaction [*Axford*, 1964]; likewise some of the potential $\Delta\varphi_{pc}$ across the polar cap in the ionosphere is owed to the viscous interaction [*Reiff et al.*, 1981]. To estimate the portion of these potentials that are owed to viscous interactions in the simulations, the measurements of the potentials under a purely northward IMF are needed to determine the contribution in the absence of low-latitude reconnection on the dayside [*Sergeev and Kuznetsov*, 1981; *Mozer*, 1984; *Weimer*, 1995; *Tsurutani and Gonzalez*, 1995]. (Another method to estimate the viscous interaction would use the measurements under zero magnetic field in the solar wind [cf. *Sonnerup et al.*, 2001; *Farrugia et al.*, 2007; *Clauer et al.*, 2007]). However, the authors are loath to trust MHD in the absence of a magnetic field (cf. J. E. Borovsky and S. P. Gary, On viscosity and the Reynolds number of MHD turbulence in collisionless plasmas: Coulomb collisions, Landau damping, and Bohm diffusion, submitted to *Physics of Plasmas*, 2008). For this assessment of the viscous interaction, a simulation from *Borovsky et al.* [2008] is examined. In this simulation the solar wind parameters are identical to the present simulations (see Table 1), except the IMF was turned from purely southward to purely northward halfway through the run. The height-integrated Pedersen conductivity was 5 mho. In Figure 11 the magnetospheric potential $\Delta\varphi_{mag}$ at X = −8 R_E and the cross–polar cap potential $\Delta\varphi_{pc}$ in the ionosphere are plotted from the *Borovsky et al.* [2008] south-to-north run. As indicated on Figure 11, the IMF was southward with B_z = −10 nT from time 0 to 85 min and was northward with B_z = +10 nT from 85 min to 165 min. About 20 min after the IMF was switched (it was switched at the sunward boundary of the simulation at X = +33 R_E) the potentials drop, eventually dropping to below 10 kV. This 10 kV is the

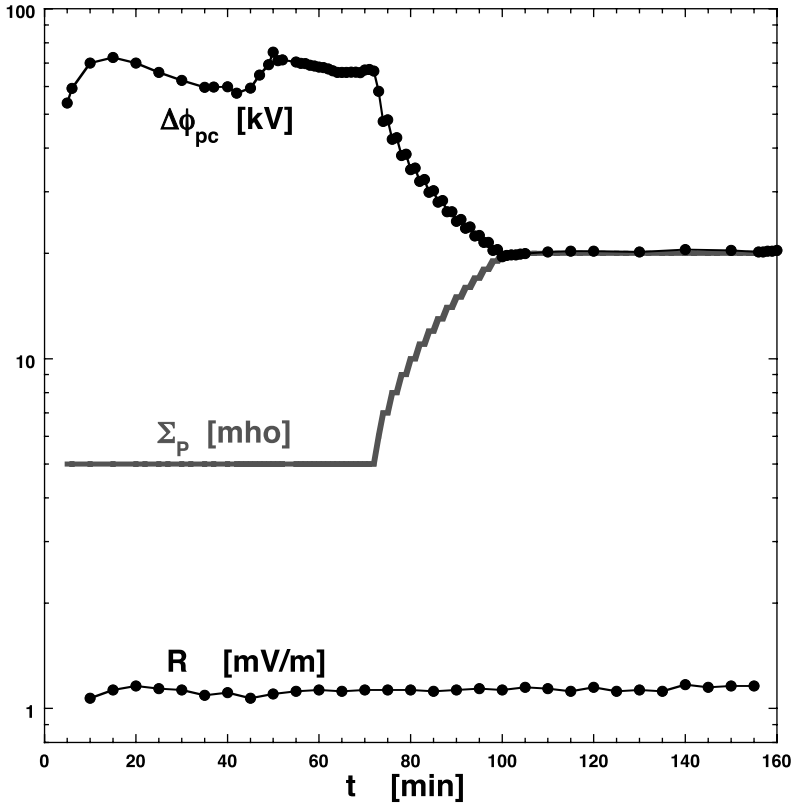

Figure 8. From the same low-resolution (near-Earth region) simulation with steady solar wind parameters that appears in Figure 1, several quantities are plotted as a function of time. The Pedersen conductivity Σ_P of the ionosphere is ramped up with time (middle curve, gray). In reaction to the increase in Σ_P, the cross–polar cap potential $\Delta\varphi_{pc}$ reduces (top curve). However, the local reconnection rate at the dayside magnetopause (bottom curve) does not change. The reconnection rate is measured at Y = +2.5 R_E. The solar wind parameters are fixed at v = 300 km s^{-1}, $B_z = -10$ nT, and n = 2 cm^{-3}.

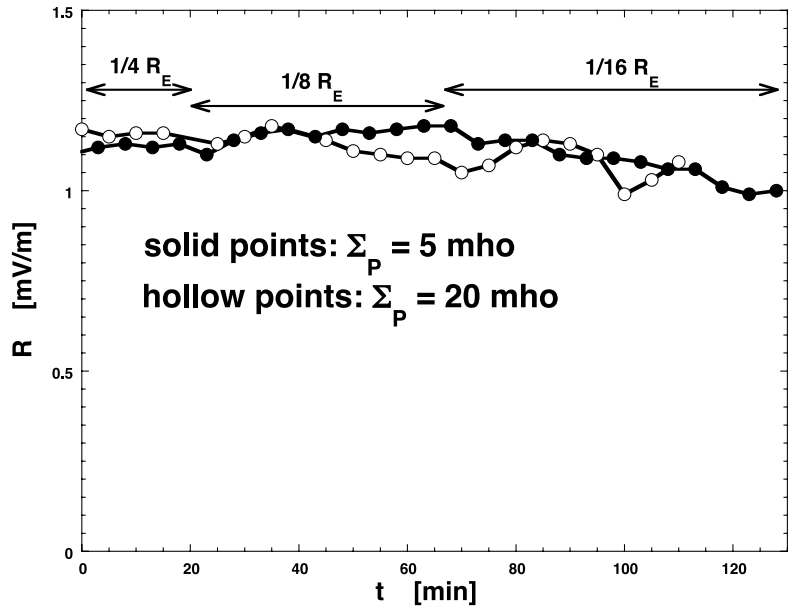

Figure 9. For the two high-resolution simulations of Figure 3, one with Σ_P = 5 mho (solid points) and one with Σ_P = 20 mho (hollow points), the local reconnection rate at the dayside magnetopause is plotted. The reconnection rate is measured at Y = +2.5 R_E. As indicated in Figure 9, the resolution of the near-Earth region in the simulations changes with time from 1/4 R_E (low) to 1/8 R_E (medium) to 1/16 R_E (high). The solar wind parameters are fixed at v = 300 km s^{-1}, $B_z = -10$ nT, and n = 2 cm^{-3}.

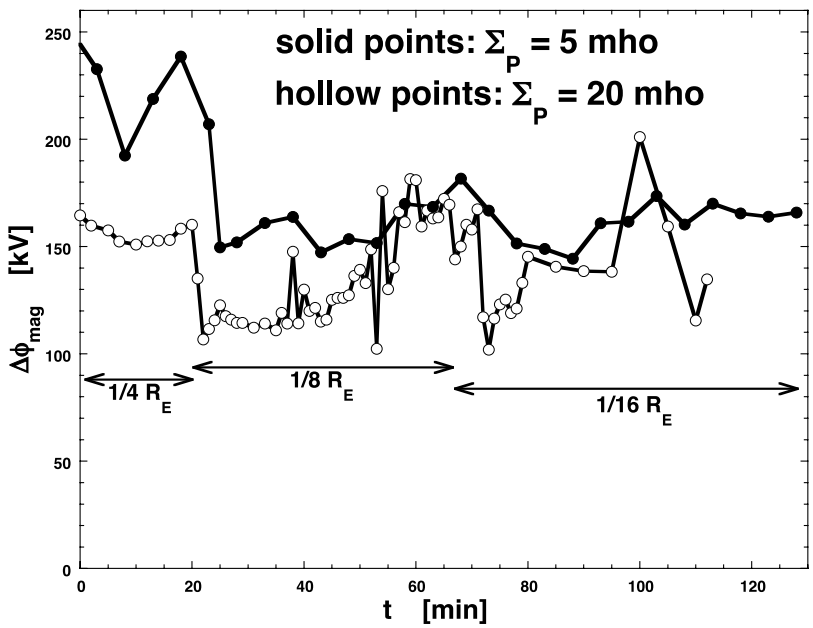

Figure 10. For the two simulations of Figure 3, one with Σ_P = 5 mho (solid points) and one with Σ_P = 20 mho (hollow points), the potential $\Delta\varphi_{mag}$ across the magnetosphere at X = −8 R_E is plotted. As indicated in Figure 10, the resolution of the near-Earth region in the simulations changes with time from 1/4 R_E (low) to 1/8 R_E (medium) to 1/16 R_E (high). The solar wind parameters are fixed at v = 300 km s^{-1}, B_z = −10 nT, and n = 2 cm^{-3}.

contribution in the simulation of the viscous interaction plus the contribution of reconnection behind the cusp. Hence, when the IMF is southward and there is low-latitude reconnection on the dayside, we estimate that the viscous contributions to both $\Delta\varphi_{mag}$ and $\Delta\varphi_{mag}$ is less than 10 kV, which is about 10% or less of the total values under southward IMF when dayside reconnection is ongoing.

[32] In these MHD simulations, there is a difference between $\Delta\varphi$ in the ionosphere and $\Delta\varphi$ across the magnetosphere. The analysis of A. J. Ridley and G. Toth (unpub-

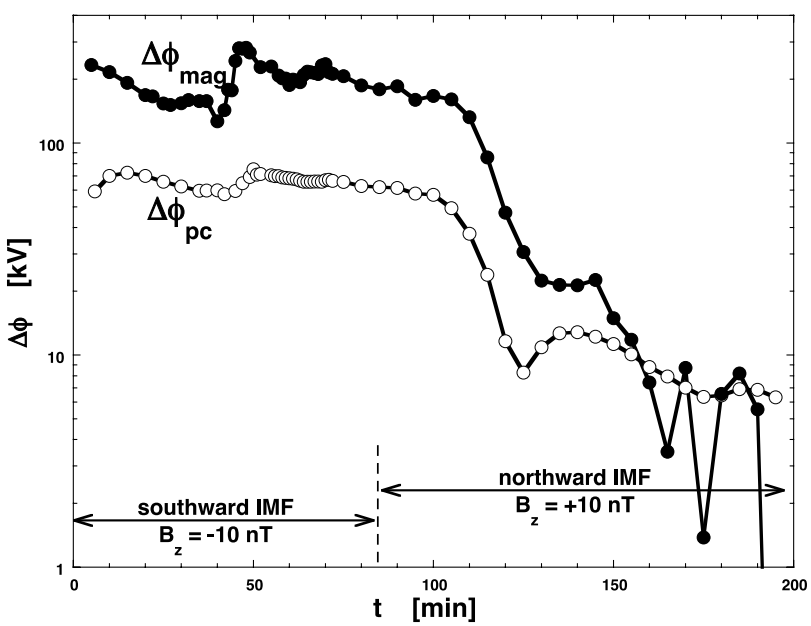

Figure 11. From a simulation of *Borovsky et al.* [2008] in which the IMF was switched from −10 nT to +10 nT at time t = 85 min, the polar cap potential $\Delta\varphi_{pc}$ in the ionosphere (hollow points) and the potential $\Delta\varphi_{mag}$ across the magnetosphere at X = −8 R_E (solid points) are plotted as functions of time. The resolution of the near-Earth region is low (1/4 R_E) and the Pedersen conductivity was Σ_P = 5 mho. The solar wind speed and density are fixed at v = 300 km s^{-1} and n = 2 cm^{-3}.

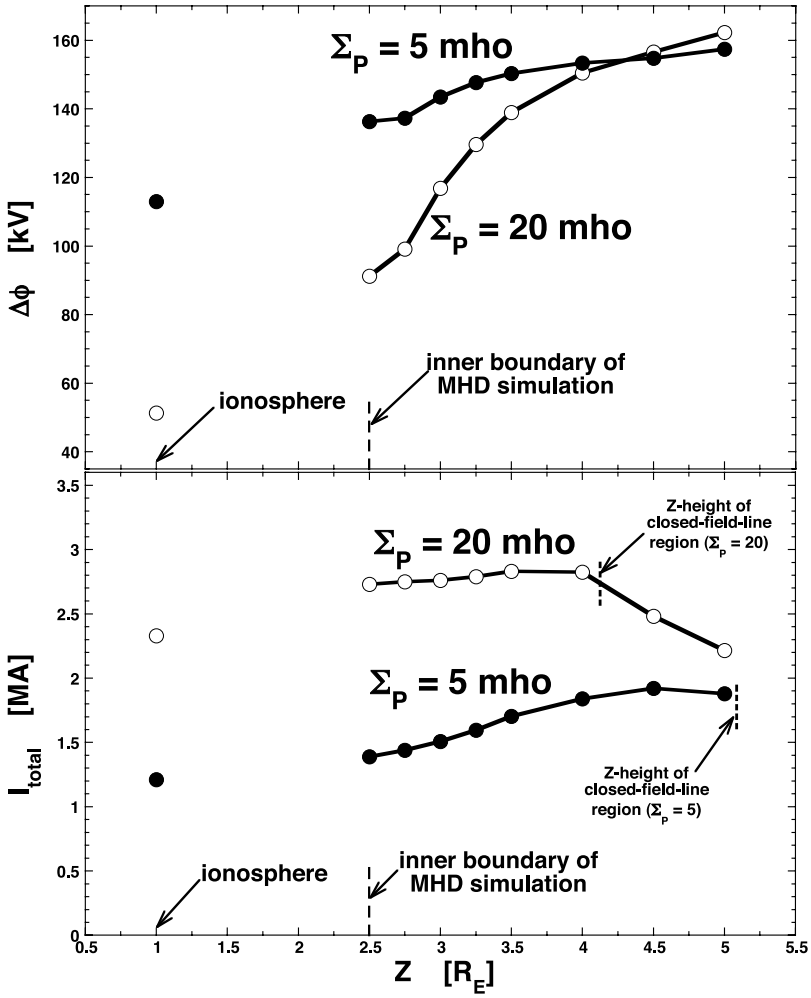

Figure 12. The mapping of the electrical potential and electric current between the magnetosphere and the ionosphere in the BATSRUS simulation. (top) The maximum potential difference in Z = constant planes from Z = 2.5 R_E to Z = 5 R_E above the northern polar cap is plotted, and (bottom) the total current flowing across the Y < 0 portion of the Z = constant planes above the northern polar cap is plotted. At Z = 1 R_E the maximum potential difference in the ionosphere is plotted in Figure 12 (top), and the net radial current into the dawnside ionosphere is plotted in Figure 12 (bottom). The solid points are from a Σ_P = 5 mho simulation, and the hollow points are from a Σ_P = 20 mho simulation. For each simulation, the height of the closed field line region of the magnetosphere is indicated: if the plane is above this height, then all of the field-aligned current from the ionosphere does not cross through this plane. For both cases, high-resolution near-Earth regions are used, and the solar wind parameters are fixed at v = 300 km s^{-1}, B_z = −10 nT, and n = 2 cm^{-3}.

lished data, 2008) indicates that $\Delta\varphi$ is underestimated in the ionosphere owing to finite grid–resolution effects. This is supported by the fact that at higher near-Earth region resolutions the polar cap potential $\Delta\varphi_{pc}$ is higher (see Figure 7 and see A. J. Ridley and G. Toth (unpublished data, 2008)). As a test, the maximum potential differences in the magnetosphere in Z = constant planes over the polar cap are calculated for two high-resolution simulations (Σ_P = 5 mho, solid points, and Σ_P = 20 mho, hollow points) and the results are plotted in Figure 12 (top). The inner boundary of the MHD simulation is at r = 2.5 R_E. Also plotted in Figure 12 (top) at Z = 1 R_E is the maximum potential differences in the ionosphere: 113 kV (for Σ_P = 5 mho) and 51 kV (for Σ_P = 20 mho). As can be seen in Figure 12 (top), the potential difference in the magnetosphere decreases as the ionosphere is approached. This measured progression supports the finite grid–resolution underestimate picture. Note that other simulations see this difference between the magnetosphere and ionosphere [e.g., *Merkine et al.*, 2003]. And note further that arguments have been made that there is a difference in potentials across the real ionosphere and real magnetosphere [*Russell et al.*, 2001]. In Figure 12 (bottom) the net current I_{total} passing through dawn half (Y < 0) of the Z = constant planes in the magnetosphere is calculated for the two simulations. This is the magnetospheric current heading for the ionosphere. As can be seen in Figure 12 (bottom), this total current appears to be fairly well conserved as the ionosphere is approached. Also

Table 4. First 14 Findings of This Study Categorized According to Properties of the Magnetosphere That Change During Polar Cap Saturation and Properties That Do Not Change[a]

	Property	Possible Reason
	Properties Affected by Increase of Σ_P	
1	Cross–polar cap potential reduced	Solar wind cannot deliver current
2	E_y reduced over polar cap	Mapping of reduced polar cap potential
3	$v_\perp$ reduced over polar cap	Mapping of reduced polar cap potential
4	Cross–polar cap currents increase	Ionospheric resistivity is lowered
8	Dayside magnetic field weakens	Perturbation from polar currents
9	Magnetopause at nose moves inward	Weakening of dayside field
12	B_x increases over polar cap	Perturbation from polar currents
13	Cusp shifts sunward	Weakening of dayside field
14	Closed field line region flattens on dayside	Weakening of dayside field
	Properties Not Affected by Increase of Σ_P	
5	Geometrical factor $I_{total}/\Sigma_P\Delta\varphi_{pc}$ unchanged	Current pattern in ionosphere unaffected
6	Dayside reconnection rate unchanged	Local plasma parameters unchanged
7	Cross-magnetosphere potential unchanged	Reconnection rate unaffected
10	Magnetopause magnetic field strength constant	Set by pressure balance with solar wind
11	Flaring at terminators does not change significantly	

[a]In the final column a possible reason why the property does or does not change is listed.

plotted in Figure 12 (bottom) at Z = 1 R_E is the net radial current going into the dawn ionosphere.

5. Changes to the Dayside Magnetosphere

[33] When the conductivity of the ionosphere increases and the polar cap potential saturates, several properties of the magnetosphere change. These properties are discussed here and noted in Table 4.

[34] In Figures 13 (top), 13 (middle), and 13 (bottom) the morphology of the currents flowing between the polar cap ionosphere and the magnetosphere is examined. In Figure 13 (top) a color contour of the logarithm of the magnitude of the current density in the X = 0 plane (as viewed from the sun) is shown. As can be seen, there are intense currents (red and yellow) flowing out of the northern and southern ionospheres in this plane. In Figure 13 (middle) the contour plot of the magnitude of the current density is redrawn with a set of magnetic field lines traced. Red field lines are closed (both foot points on the Earth), black field lines are open (one foot point on the Earth), and blue field lines are solar wind field lines (not connected to Earth). As can be seen by comparing Figures 13 (top) and 13 (middle), the strong currents from the ionosphere flow (1) at the boundary of the open-closed field regions and (2) in the open field region near the open-closed boundary. In Figure 13 (bottom) the Y component of the current density j_y is plotted in the Y = +5 R_E plane in the duskside of the magnetosphere. As can be seen, j_y is positive in both the northern and southern hemispheres, indicating that the current is in the dawn-to-dusk (Region-I) sense in both the northern and southern hemispheres. Note in Figure 13 (bottom) that the current is skewed toward the nightside of the dawn-dusk terminator. This skewing toward nightside is more pronounced in the simulations with higher resolution in the near-Earth region than it is in simulations with lower resolution.

[35] In Figure 14 the radial profile of the magnetospheric magnetic field along the sun-Earth line is plotted for two high-resolution simulations: one with Σ_P = 5 mho (black curve) and one with Σ_P = 20 mho (gray curve). The dotted curve is the dipole magnetic field strength. The magnetic field strength in the dayside magnetosphere tends to be compressed to a strength that is greater than the dipole strength [e.g., *Hones*, 1963; *Cahill and Amazeen*, 1963]. As can be seen in Figure 14, the strongly saturated run (Σ_P = 20) has a dayside magnetic field strength that is reduced from the weakly saturated (Σ_P = 5) case. In fact the dayside magnetic field strength in the saturated case is below the dipole strength. This weakening of the dayside magnetic field as the polar cap conductivity increases is noted in Table 4. (Note that a weakening of the dayside magnetic field for polar cap saturation produced by changing the solar wind parameters was observed in the simulations of *Siscoe et al.* [2004]). For both curves in Figure 14 the magnetopause magnetic field strength can be seen at the "knee" where the plotted curve drops suddenly in magnitude; in both cases the magnetic field strengths at the magnetopause are the same. Note that although the magnetic field strength is weakened on the dayside owing to polar cap saturation, the field strength at the magnetopause is not [see also *Lavraud and Borovsky*, 2008]. This magnetopause field strength is determined by pressure balance with the solar wind and the solar wind is not changed. The constancy of the magnetopause magnetic field strength while the ionospheric conductivity increases is noted in Table 4. Note however that the position of the magnetopause moves inward closer to the Earth when the dayside field strength is weakened.

[36] In Figure 15 the shape of the magnetopause ($B_z \approx 0$ region) is shown in the equatorial plane in a snapshot from for the Σ_P = 5 mho (Q $\approx$ 1) simulation (solid points) and from the Σ_P = 20 mho (Q $\approx$ 4) simulation (hollow points). High-resolution near-Earth regions are used and as always the solar wind parameters are identical. As can be seen in Figure 15, the position of the magnetopause is closer to the Earth at the nose in the Σ_P = 20 mho case than it is in the Σ_P = 5 mho case, as anticipated from the discussion above about Figure 14. Also, as can be seen, the position of the magnetopause is closer to the Earth at the terminator in the Σ_P = 20 mho case than it is in the Σ_P = 5 mho case. These trends are elaborated in Figure 16, where the distance to the magnetopause at the nose (bottom curves) and at the terminator (top curves) is plotted as functions of time for the Σ_P = 5 mho (solid points) and Σ_P = 20 mho (hollow

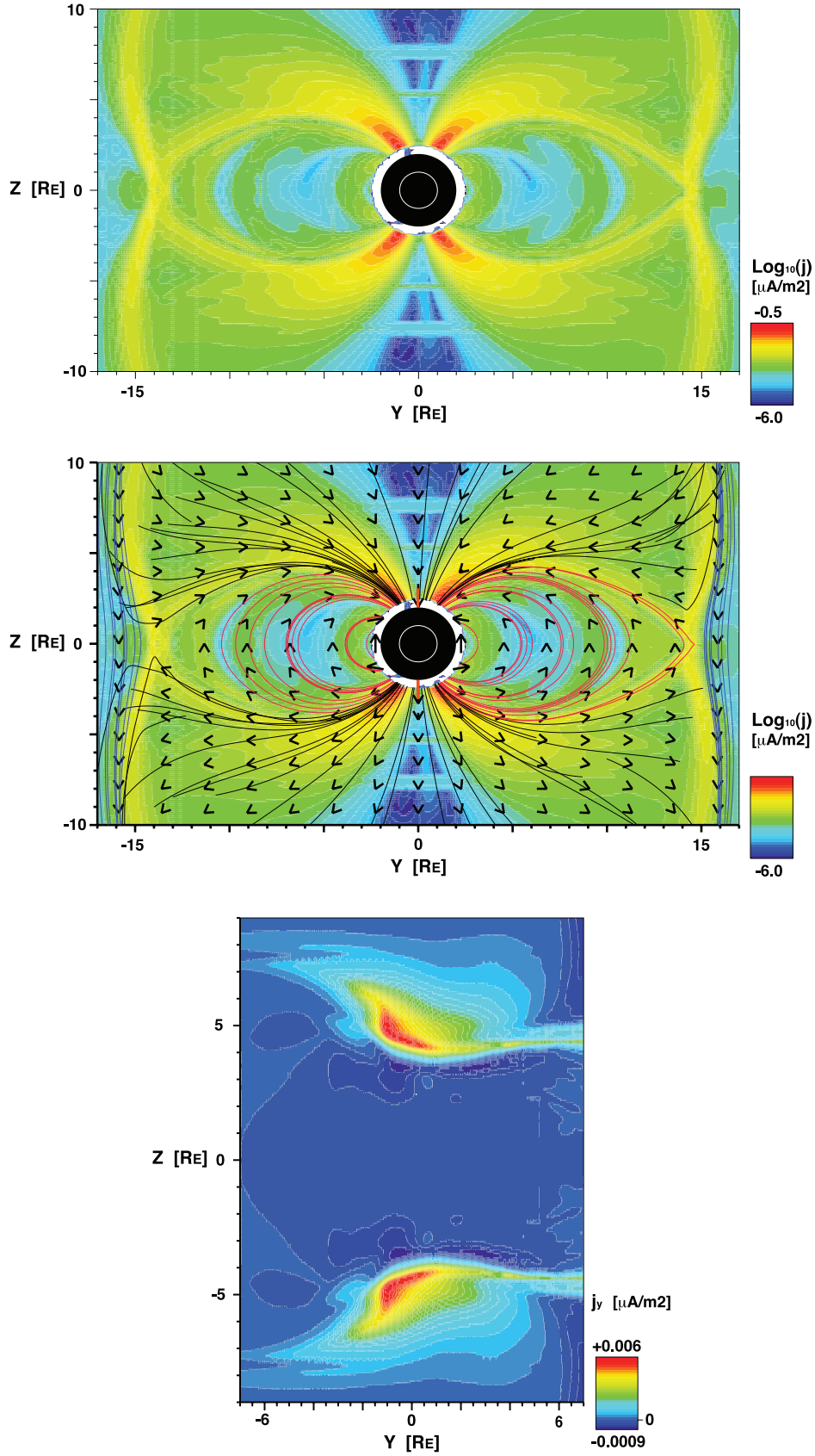

Figure 13. From a simulation with a high-resolution near-Earth region and with $\Sigma_P = 20$ mho, (top) the total current density in the dawn-dusk terminator plane (X = 0) is plotted in color. (middle) It is replotted with traced magnetic field lines overlayed, and (bottom) the y component current density j_y flowing through the Y = +5 R_E plane in the dusk sector is plotted in color.

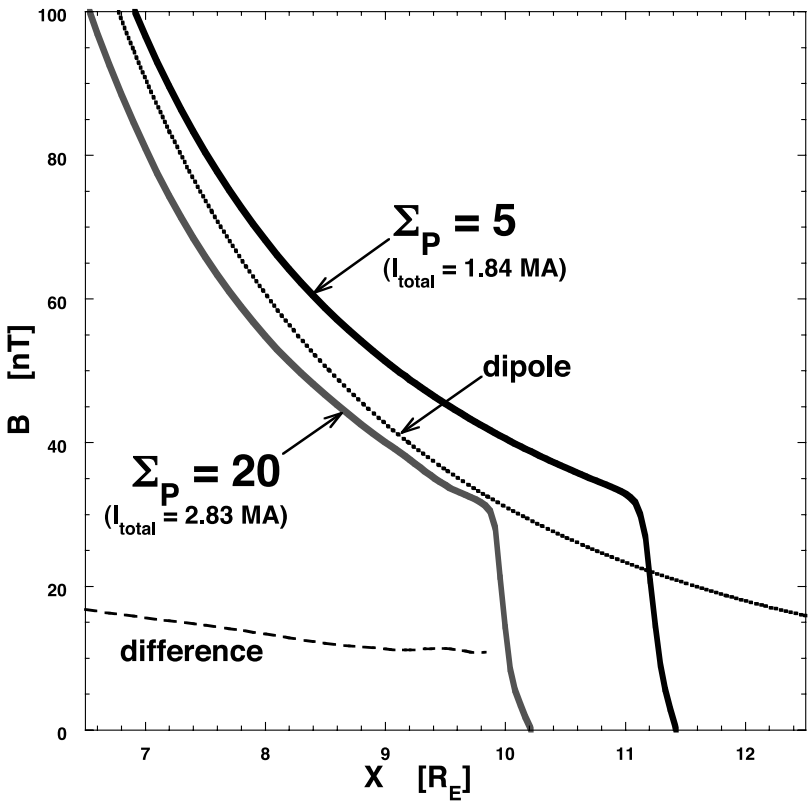

Figure 14. For two simulations with high-resolution near-Earth regions, one with $\Sigma_P = 5$ mho (heavy black curve) and one with $\Sigma_P = 20$ mho (heavy gray curve), the magnetic field strength B is plotted along the sun-Earth line. Note the position of the magnetopause in the two curves where they suddenly turn downward. The strength of the dipole field is plotted as the dotted curve, and the values of the $\Sigma_P = 20$ curve subtracted from the values of the $\Sigma_P = 5$ mho curve are plotted as the dashed line.

points) simulations. The grid resolution over the pole (and throughout the near-Earth region) changes with time as noted by the horizontal arrows in Figure 16. As can be seen, when the resolution is high (so that the cross–polar cap currents are strongest) the magnetopause at the nose is moved inward for the $\Sigma_P = 20$ mho (fully saturated) simulation. The difference in positions at the nose is about 1 R_E. The inward movement of the magnetopause at the nose as the ionospheric conductivity increases is noted in Table 4. The magnetopause at the terminator is also moved slightly inward for the $\Sigma_P = 20$ mho simulations. The difference in positions of the magnetopause at the terminator (top curves in Figure 16) is less than 1 R_E. Notice the fluctuations in the measured position of the magnetopause at the terminator in Figure 16 owing to Kelvin-Helmholtz waves (as seen in Figure 15).

[37] In Figure 17 the X component of the magnetic field B_x is plotted as a function of Z above the Northern polar cap along the (X, Y) = (0, 0) line for the weakly saturated ($\Sigma_P = 5$ mho, $Q \approx 1$) and the strongly saturated ($\Sigma_P = 20$ mho, $Q \approx 4$) cases. The total current flowing between the ionosphere and magnetosphere is I_{total} noted in Figure 17 at the time at which each case is plotted. For a purely dipole field, B_x is zero everywhere along this (X, Y) = (0, 0) line. As can be seen, the B_x perturbation is largest near the Earth (near the current system) and decreases with increasing Z. Also, the perturbation is larger when the total current I_{total} is larger, which is in the more saturated $\Sigma_P = 20$ mho case. Over the southern polar cap (-Z) the B_x perturbations are similar, except that the sign is reversed. This increase of B_x over the polar cap as the ionospheric conductivity increases is noted in Table 4.

[38] Applying Ampere's (Biot-Savart) law for the currents flowing into and across the polar cap provides a crude agreement with the differences in the magnetic field of the magnetosphere seen between the $\Sigma_P = 5$ mho and $\Sigma_P = 20$ mho simulations. In Figure 17, in the weak-saturation ($\Sigma_P = 5$ mho, $Q \approx 1$) case the total current flowing out of one polar cap is $I_{total} = 1.84 \times 10^6$ A and in the strong-saturation ($\Sigma_P = 20$ mho, $Q \approx 4$) case the total current flowing out of one polar cap is $I_{total} = 2.83 \times 10^6$ A. Doubling the currents to account for the northern and southern hemispheres, and subtracting yields a difference of 2.0×10^6 A between the two cases. Ampere's law for a simple line current of 2.0×10^6 A at a distance of 5 R_E yields a magnetic field perturbation of 12.6 nT. In Figure 17 at Z = 5 R_E the difference between the B_x values for the high-resolution strong saturation and the high-resolution weak saturation is 23 nT, which is about double the 12.6 nT Ampere's law estimate. A better accounting of the morphology of this current (see Figure 13 (top)) raises the Ampere's law estimate by $\sim 2^{1/2}$ providing a better agreement to the observed field difference. Similarly in Figure 14, the difference in B_z values between the strong-saturation and the

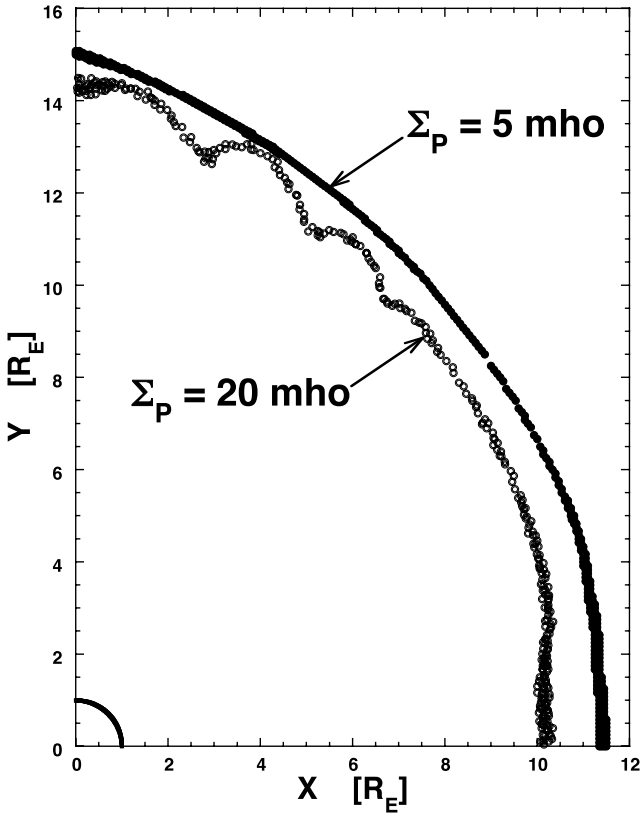

Figure 15. The position of the magnetopause is shown for two high-resolution (near-Earth region) simulations: once for a Σ_P = 5 mho (solid points) simulation and once for a Σ_P = 20 mho (hollow points) simulation. In the Z = 0 plane, points are collected where -5 nT < B_z < 5 nT, and those points are plotted in Figure 15. In both simulations, the solar wind parameters are identical: v = 300 km s^{-1}, B_z = -10 nT, and n = 2 cm^{-3}.

weak-saturation cases at X = 5 R_E is 21 nT, which is again about double the 12.6 nT Ampere's law estimate. Here a better accounting of the morphology of this current (see Figure 13 (top)) reduces the Ampere's law estimate yielding a worse agreement with the observed field difference.

[39] In Figure 18 (top) the X component of the magnetic field B_x is plotted in color in the X = 0 (dawn-dusk) plane, with some magnetic field lines traced. The snapshot is from a strong-saturation (Σ_P = 20 mho) simulation with the high-resolution near-Earth region. Red and yellow is a positive (sunward) field and blue is a negative (antisunward) field. As can be seen, there is a shift in the sign of B_x across the open-closed magnetic field line boundary. In the northern lobe B_x is positive and in the southern lobe B_x is negative. This shift in the magnetic field direction across the open-closed boundary is akin to the observed change in flaring angles between the plasma sheet (closed) and lobe (open) regions in the magnetotail, with a Region-I sense current flowing in the magnetotail on the plasma sheet/lobe boundary [*Birn*, 1989; *Candidi et al.*, 1990].

[40] In Figure 18 (bottom) the perturbation Z component of the magnetic field $\delta B_z = B_z - B_{zdipole}$ is plotted in color in the Y = 0 (noon-midnight) plane. Yellow is a positive (northward) perturbation and blue is a negative (southward) perturbation. As can be seen, in the dayside magnetosphere the perturbation is negative, producing a depression of the magnetic field below the dipole strength, even in the presence of compression from the solar wind (see also Figure 17). This weakening of the dayside magnetic field with increasing ionospheric conductivity is noted in Table 4. And as can be seen, in the nightside magnetosphere the perturbation is positive, producing an increase of the magnetic field above the dipole strength, even in the presence of stretching in the magnetotail.

[41] This reduction of the dayside magnetic field when the polar cap saturation is strong is confirmed in Figure 19 where magnetic field measurements from the GOES-10 spacecraft are shown in the noon local time sector of geosynchronous orbit (6.6 R_E) near the equator. To ensure that the GOES spacecraft was not in the magnetosheath owing to magnetopause crossings, GOES magnetometer measurements were only used if the magnetic field clock angle measured by GOES was within 20° of the dipole direction. (Magnetopause crossings at geosynchronous orbit almost always occur under southward IMF [e.g., *Rufenach et al.*, 1989], which would put the clock angle in the magnetosheath at 90° or more from the dipole direction.) Once per day for the years 1999–2003, a 40-min average of the geosynchronous magnetic field strength is made centered on local noon. At the time of each geosynchronous magnetic field measurement, the OMNI2 data set [*King and Papitashvili*, 2005] is used to determine the total pressure of the solar wind (ram pressure ρv^2 plus magnetic pressure $B^2/8\pi$). If a geomagnetic storm was on (Kp > 4.5), then the magnetic pressure $B^2/8\pi$ measured at (noon) geosynchronous orbit is plotted as a function of the solar wind pressure in Figure 19 (black points). Using the OMNI2 data set to calculate the Alfven speed v_A of the solar wind and using F10.7 values to estimate Σ_P with $\Sigma_P = 0.77\ F_{10.7}^{1/2}$ [*Ober et al.*, 2003], the polar cap saturation parameter $Q = v_A\Sigma_P/806$ (expression (2)) is calculated. Geosynchronous magnetic field measurements taken when Kp > 4.5 and when Q has an extreme value are plotted as the colored points: blue when Q is very low (Q < 0.75) and red when Q is very high (Q > 2). As can be seen in Figure 19, when Q is high (polar cap saturation) the geosynchronous magnetic field strength at noon tends to be lower than when Q is low (polar cap not saturated). The horizontal green line indicates the value of $B^2/8\pi$ for a dipole field at 6.6 RE. Note that when polar cap saturation is ongoing (red points) the field can be depressed below the dipole strength, as Figure 14 and Figure 18 (bottom) indicate.

[42] As polar cap saturation deepens, the cusps of the magnetosphere move equatorward. This can be seen by comparing Figures 20 (top) and 20 (bottom). Figure 20 (top) is a cut of the magnetosphere at local noon for Σ_P = 5 mho and Figure 20 (bottom) is a cut for Σ_P = 20 mho. Both cases have high-resolution near-Earth regions. The color represents plasma flow speed and magnetic field lines are traced. Focusing on the boundary between open (black) and closed (red) field lines, the boundary is shifted about 4° equatorward at r = 3 R_E in Figure 20 (bottom) (Σ_P = 20 mho) relative to the boundary's position at r = 3 R_E in Figure 20 (top) (Σ_P = 5 mho). This equatorward shift of the cusps with increasing ionospheric conductivity is noted in Table 4.

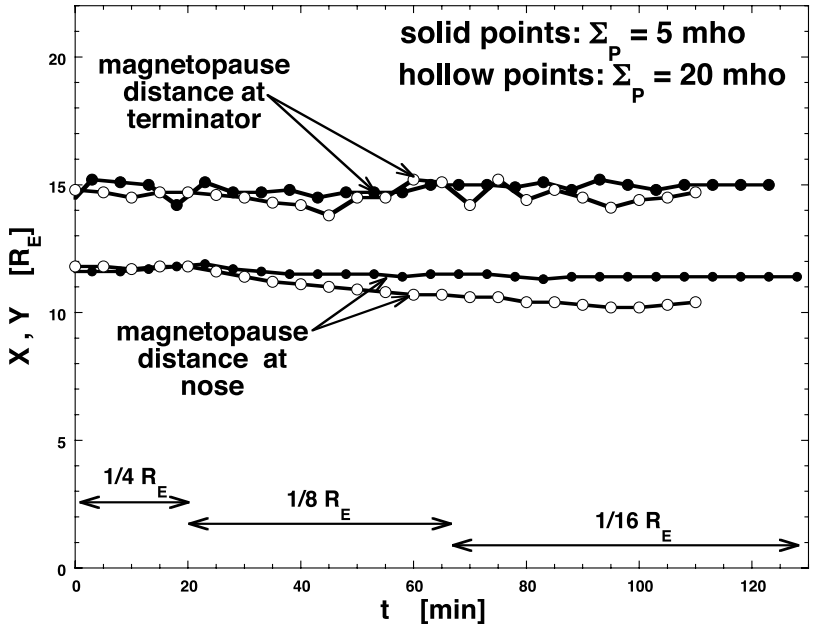

Figure 16. For the two simulations of Figure 3, one with Σ_P = 5 mho (solid points) and one with Σ_P = 20 mho (hollow points), the distance to the magnetopause along the sun-Earth line (bottom curve) and the distance to the magnetopause at the dusk terminator (top curve) is plotted. As indicated in Figure 16, the resolution of the near-Earth region in the simulations changes with time from 1/4 R_E (low) to 1/8 R_E (medium) to 1/16 R_E (high). The solar wind parameters are fixed at v = 300 km s^{-1}, $B_z = -10$ nT, and n = 2 cm^{-3}.

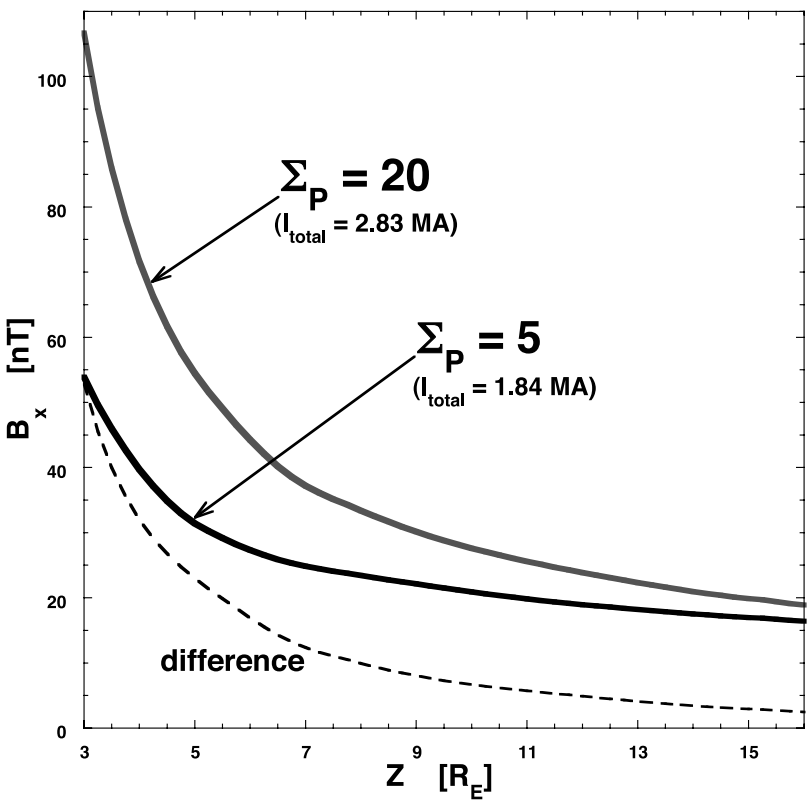

Figure 17. For two simulations with high-resolution near-Earth regions, one with Σ_P = 5 mho (heavy black curve) and one with Σ_P = 20 mho (heavy gray curve), the x component of the magnetic field B_x is plotted over the northern polar cap along the (X,Y) = (0,0) line as a function of Z. The values of the Σ_P = 5 curve subtracted from the values of the Σ_P = 20 mho curve are plotted as the dashed line.

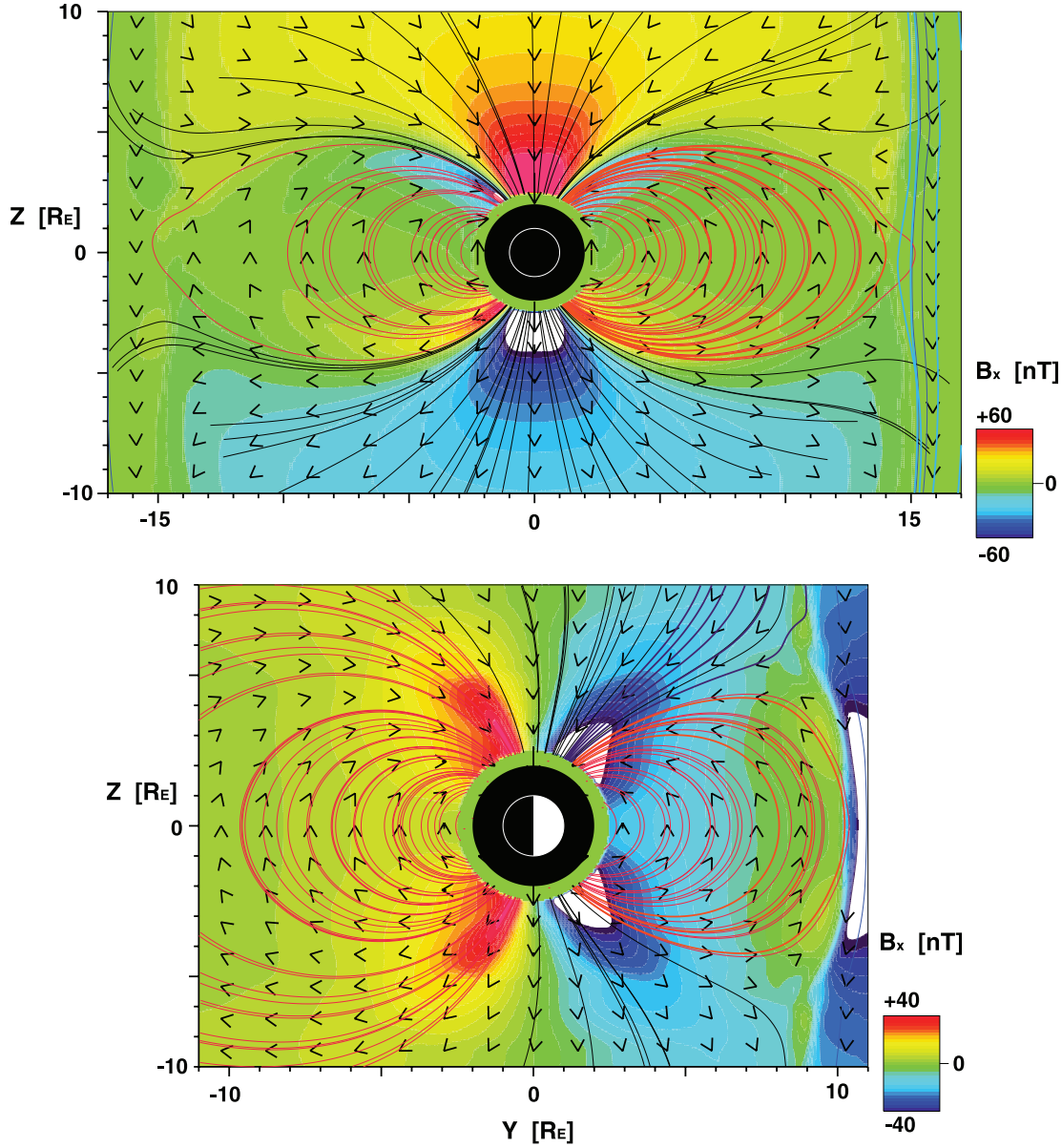

Figure 18. For a high-resolution (near-Earth region) simulation with Σ_P = 20 mho, (top) the x component magnetic field B_x is plotted in color in the dawn-dusk terminator (X = 0) plane, and (bottom) the difference between the z component magnetic field B_z and the B_z of a dipole is plotted in the noon-midnight (Y = 0) plane. A sampling of magnetic field lines are traced to demark the closed field line region (red field lines) from the open field line region (black field lines).

[43] As polar cap saturation deepens the dipolar region of the magnetosphere on the dayside flattens. In Figure 20 (bottom) (Σ_P = 20 mho) the closed field line region of the magnetosphere (red field lines) is restricted to lower values of |Z| than is the closed field line region in Figure 20 (top) (Σ_P = 5 mho). For cases with high-resolution near-Earth regions, the closed field line regions of the Σ_P = 20 mho simulations are confined to Z ≈ ±4 R_E at noon whereas the closed field line regions of the Σ_P = 5 mho simulations are confined to Z ≈ ±5.5 R_E. This flattening of the closed field line region on the dayside is explored further in Figure 21 where cuts of the magnetosphere at the dusk terminator are shown for Σ_P = 5 mho (Figure 20 (top)) and Σ_P = 20 mho (Figure 20 (bottom)). As can be seen, at the terminator the closed field line region of the magnetosphere (red field lines) is restricted to lower values of |Z| for Σ_P = 20 mho than it is for Σ_P = 5 mho. For the cases in Figure 21 (with high-resolution near-Earth regions), the closed field line regions of the Σ_P = 20 mho simulation is confined to Z ≈ ±4.5 R_E at dusk whereas the closed field line regions of the Σ_P = 5 mho simulation are confined to Z ≈ ±5.5 R_E. This flattening of the closed field line region of the dayside magnetosphere with an increase in polar cap saturation is noted in Table 4. Note the taillike stretching of the closed field lines in the dawn terminator for the Σ_P = 20 mho case. The solar wind parameters for the occurrence of global sawtooth oscillations are similar to the parameters for polar cap saturation [*Borovsky and Denton*, 2006a] and that the

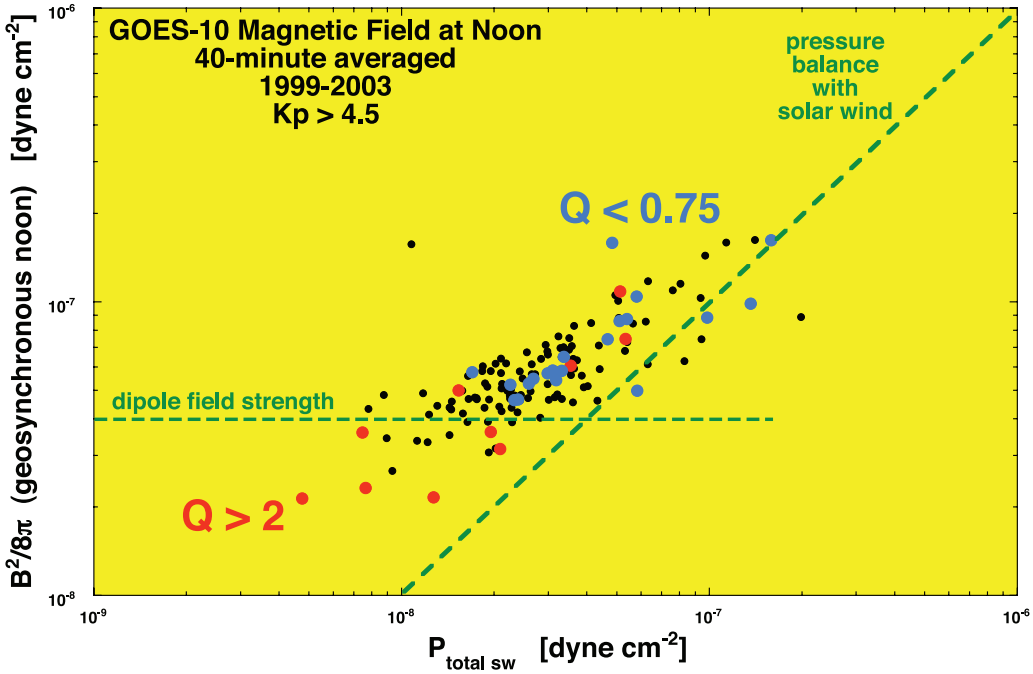

Figure 19. The measured magnetic field strength at noon geosynchronous orbit (vertical) is plotted as a function of the total pressure of the solar wind (horizontal). The geosynchronous field strength is obtained by averaging GOES-10 magnetic field measurements over a 40-min window centered on local noon. The solar wind total pressure is obtained from the OMNI2 data set. Only measurements that occurred when Kp > 4.5 are plotted. All Kp > 4.5 points are plotted in black. For each point the polar cap saturation factor Q is calculated from OMNI2 and F10.7. If Q < 0.75, the point is overplotted in blue, and if Q > 2, the point is overplotted in red. Pressure balance with the solar wind is indicated by the diagonal dashed line, and the strength of the dipole field is indicated by the horizontal dashed line.

precursor to global sawtooth oscillations is a taillike stretching of the dipole field lines in the dayside magnetosphere [*Borovsky*, 2004]. This stretching of the dipole is undoubtedly related to a flattening in Z of the closed field line region [*Borovsky et al.*, 2004].

6. Discussion: Some Observations About Polar Cap Saturation

[44] In this section, three topics are discussed: (1) the constancy of the dayside reconnection rate, (2) how the polar cap saturation in the simulations acts like a current-limited voltage generator, and (3) a circuit analysis of the polar cap saturation behavior seen in the simulations.

6.1. Dayside Reconnection

[45] In this paper the phenomenology of polar cap saturation is studied by holding the solar wind parameters fixed and varying the ionospheric conductivity. It is clear from the analysis in section 3 that the reconnection rate at the dayside magnetosphere does not change as the polar cap undergoes saturation. Neither the local reconnection rate nor the global reconnection rate change. This constancy of the reconnection rate makes sense. The reconnection rate at the magnetopause is governed by four plasma parameters at the magnetopause [*Borovsky et al.*, 2008]: the magnetic field strength B_m on the magnetospheric side, the magnetic field strength B_s on the magnetosheath side, the plasma mass density ρ_m on the magnetospheric side, and the plasma mass density ρ_s on the magnetosheath side. In order to change the reconnection rate at the dayside magnetosphere something must act to change those local plasma parameters. In the simulations, no physical processes that could change those parameters is observed.

6.2. Current-Limited Voltage Generator

[46] In Table 5, the degree by which of some key parameters of the simulations vary during the polar cap saturation process are calculated. The values of these key parameters are obtained from Table 2. The variation is expressed in terms of the ratio of the value during the Σ_P = 20 mho case to the value during the Σ_P = 5 mho case, and the ratio is calculated separately for the low-resolution, medium-resolution, and high-resolution near-Earth regions. In the first column of Table 5 the ratio of Pedersen conductivities Σ_P is listed. Σ_P varies by a factor of 4

Figure 20. For two high-resolution (near-Earth region) simulations, the morphology of the dayside magnetosphere is explored with plots in the noon meridianal plane (Y = 0). (top) A Σ_P = 5 mho simulation and (bottom) a Σ_P = 20 mho simulation. The color coding is the flow speed of the plasma. A sampling of magnetic field lines are traced to demark the closed field line region (red field lines) from the open field line region (black field lines).

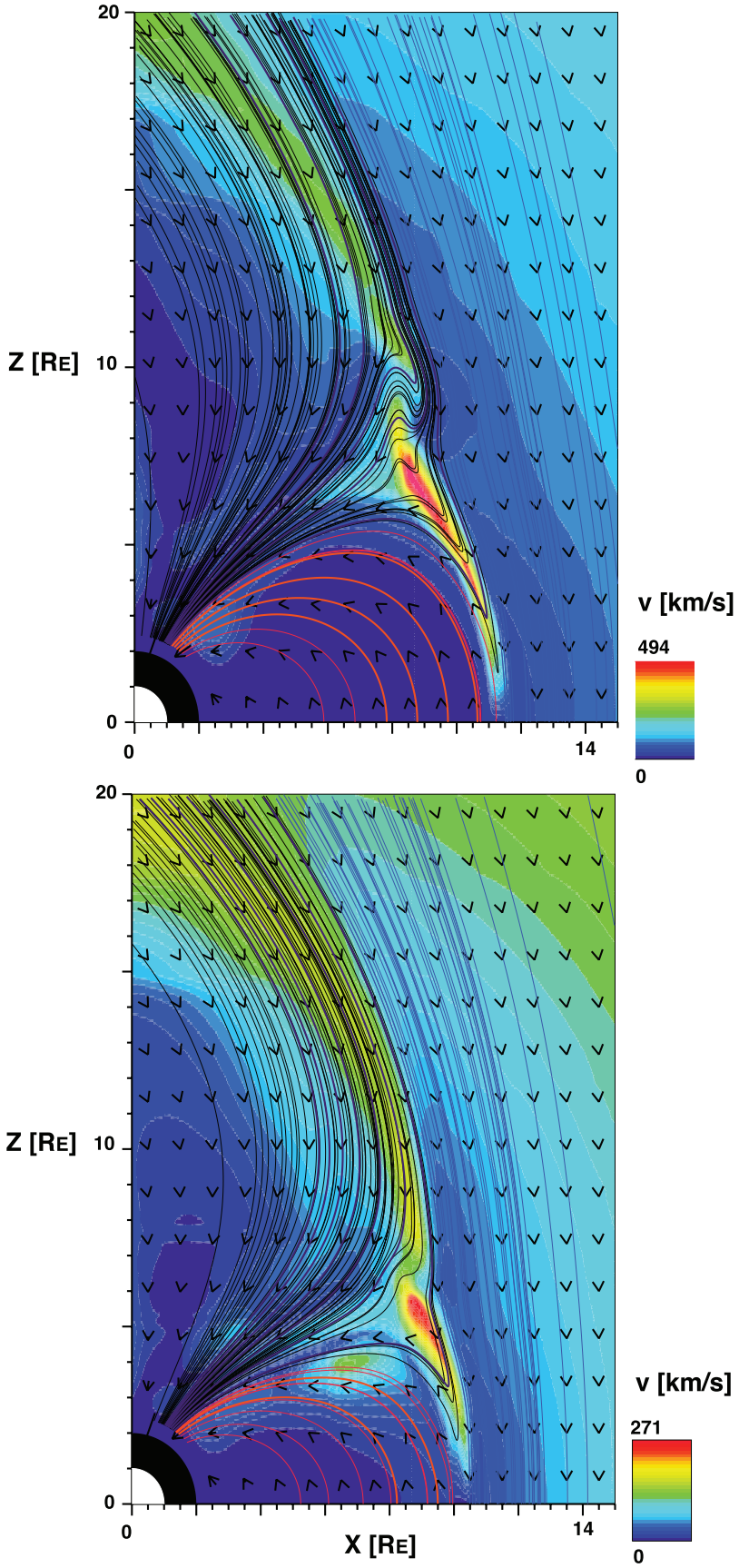

Figure 20

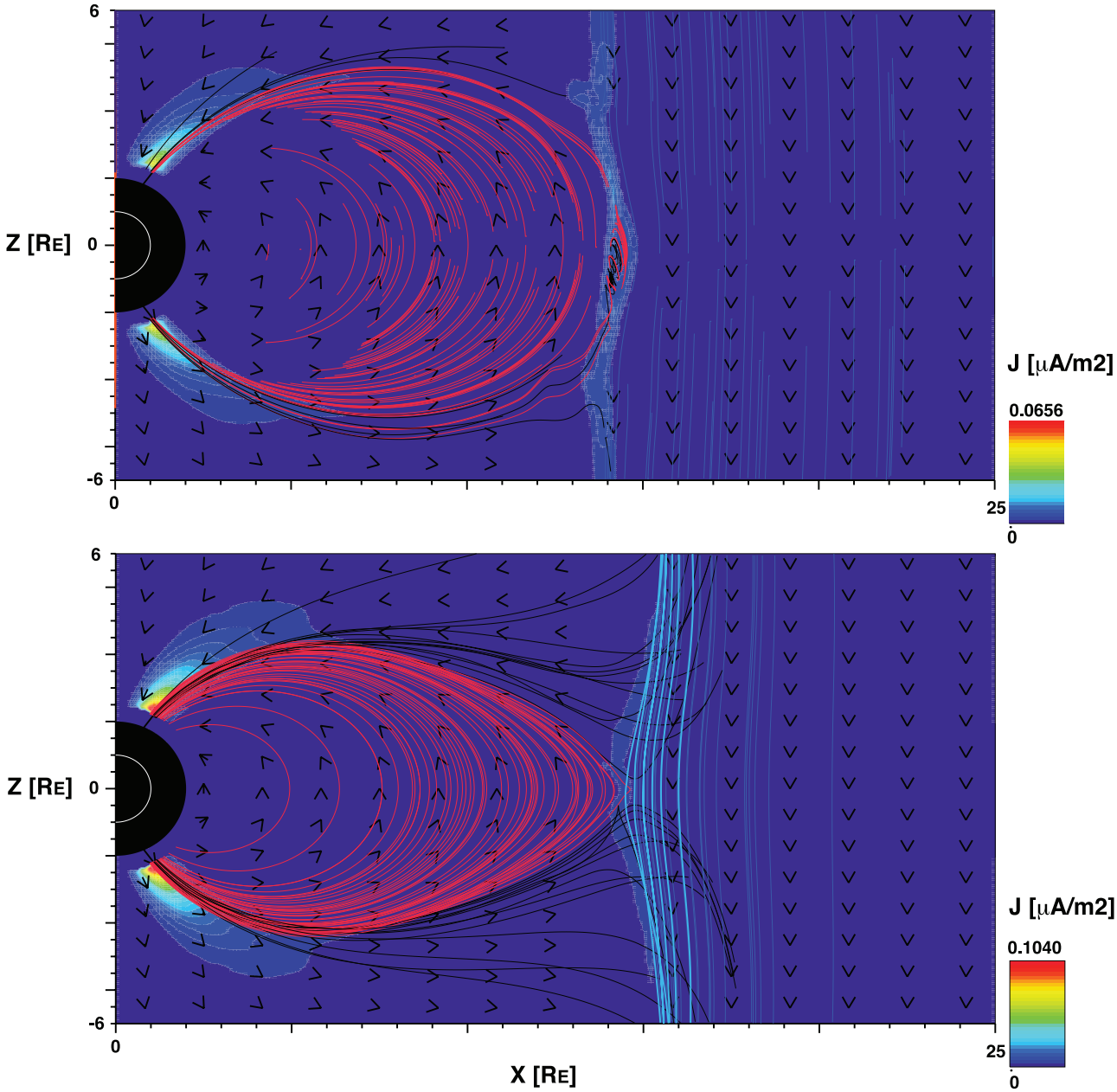

Figure 21. For two high-resolution (near-Earth region) simulations, the flattening of the closed field line region at the terminator is explored with plots in the X = 0 plane in the dusk sector as viewed from the sun. (top) A $\Sigma_P = 5$ mho simulation and (bottom) a $\Sigma_P = 20$ mho simulation. The color coding is the absolute value of the current density in the plasma. A sampling of magnetic field lines are traced to demark the closed field line region (red field lines) from the open field line region (black field lines) form the solar wind (blue field lines). The magnetosheath is also shown.

between the two cases. In the second column of Table 5 the ratio of measured polar cap potentials $\Delta\varphi_{pc}$ is listed. At high resolution $\Delta\varphi_{pc}$ varies by a factor of 2.2. In the third column the ratio of the cross–polar cap current I_{total} is listed. At high resolution I_{total} varies by a factor of 1.5, which is less than the variation in $\Delta\varphi_{pc}$. In the fourth

Table 5. Degree Over Which the Various Key Parameters Varying Between the $\Sigma_P = 5$ mho and $\Sigma_P = 20$ mho Simulations Are Compared

Grid Resolution	$\Sigma_P(20)/\Sigma_P(5)$	$\Delta\varphi_{pc}(5)/\Delta\varphi_{pc}(20)$	$I_{total}(20)/I_{total}(5)$	$\Delta\varphi_{mag}(5)/\Delta\varphi_{mag}(20)$	R(5)/R(20)
Low	4	3.35	1.16	1.46	1.04
Medium	4	2.41	1.65	1.03	1.03
High	4	2.22	1.55	1.11	0.99

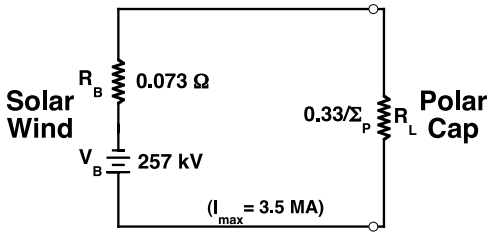

Figure 22. The circuit analyzed to represent the current-limited voltage generator (solar wind) driving the northern ionosphere is sketched. For the simulations analyzed, the values of the battery voltage V_B, the battery internal resistivity R_B, and the resistivity of the load R_L are indicated. The two values of R_L explored were 0.067Ω (Σ_P = 5 mho) and 0.0165Ω (Σ_P = 20 mho). The values obtained pertain to the solar wind parameters v = 300 km s^{-1}, $B_z = -10$ nT, and n = 2 cm^{-3}. The values of the solar wind voltage V_B and internal resistivity R_B will vary with solar wind parameters. Owing to the finite resolution of the simulations, 257 kV is an underestimate of the true voltage.

column of Table 5 the ratio of measured magnetospheric potentials $\Delta\varphi_{mag}$ is listed. At high resolution $\Delta\varphi_{mag}$ varies by only a factor of 1.11. It is essentially constant. Finally, in the fifth column of Table 5 the ratio of measured reconnection rates R at the dayside magnetopause is listed. At high resolution R varies by only a factor of 0.99. It is essentially constant. Comparing the degree of variability of the polar cap potential $\Delta\varphi_{pc}$ and the polar cap current I_{total} in Table 5: the polar cap potential varies much more than the polar cap current does. This indicates a behavior wherein the solar wind driving the ionosphere acts as does a voltage generator that is reaching the limit on its ability to deliver current [see also *Fedder and Lyon*, 1987]: the voltage droops greatly while the current into the load increases only slightly.

6.3. Circuit Analysis of the Simulations

[47] Using the analogy of a current-limited voltage generator, a circuit analysis of the solar wind driving one ionosphere can be performed. This circuit is drawn in Figure 22: the solar wind generator is depicted on the left as a battery with an internal resistance (current-limiting resistor) and the ionospheric load is depicted on the right as a simple resistance. Denoting the open circuit (zero-current) voltage of the battery (solar wind) as V_B, the current in the circuit as I, the internal resistance of the battery as R_B, and the resistance of the load as R_L, Kirchoff's law gives the expression

$$V_B = I(R_B + R_L). \tag{5}$$

[48] In the circuit of Figure 22, when the load resistance changes, the current through the circuit changes and the voltage drop across the load changes but the voltage of the battery and the internal resistance of the battery do not change. The resistivity R_L of the ionospheric load is evaluated from the simulations as follows. Ohm's law in the ionosphere can be written $R_L = V_L/I$, where V_L is the voltage $\Delta\varphi_{pc}$ across the ionosphere (load) and I is the current I_{total} flowing in the ionosphere. In section 3 it was found that the ratio $I_{total}/\Sigma_P\Delta\varphi_{pc}$ = W/L is nearly constant (see Table 2 and Figure 7) and equal to approximately 3.0. Thus, $R_L = V_L/I = \Delta\varphi_{pc}/I_{total} = W/\Sigma_P L = 1/3.0\Sigma_P$ is the resistivity of the ionosphere as a function of Σ_P. This is expressed as

$$R_L = 0.33/\Sigma_P. \tag{6}$$

[49] In Table 6 the two values of R_L are entered for the two values 5 mho and 20 mho of Σ_P utilized in the simulations. Also in Table 6, the measured values of the current I flowing through the ionosphere for the two cases are entered; these values for the high-resolution near-Earth region simulations are obtained from Table 2. With R_L and I known, expression (5) has two unknowns: V_B and R_B. Evaluating expression (5) twice (using the two sets of values in Table 6) allows V_B and R_B to be determined. It is instructive to do this. Thus, we write down expression (5) twice: once $V_B = I_1 (R_B + R_{L1})$ for case 1 (top row of Table 6) and again $V_B = I_2(R_B + R_{L2})$ for case 2 (bottom row of Table 6). Subtracting the second of these expressions from the first to eliminate V_B and then solving for R_B yields the expression

$$R_B = (I_1 R_{L1} - I_2 R_{L2})/(I_2 - I_1). \tag{7}$$

[50] Using the values in Table 6 to evaluate expression (7) yields R_B = 0.0733Ω as the value of the internal resistance of the solar wind battery. Using this value of R_B in expression (5) with R_L and I from either case 1 or case 2 of Table 6 yields V_B = 257 kV as the voltage of the solar wind generator. These values of R_B and V_B, along with expression (6) for R_L are added on to the circuit sketch of Figure 22.

[51] The maximum current that the solar wind generator could supply to the ionosphere is obtained by setting $R_L = 0$ in expression (5) (which by expression (6) is equivalent to setting $\Sigma_P \to \infty$). For V_B = 257 kV, R_B = 0.0733Ω, and $R_L = 0$, expression (5) gives I_{max} = 3.51 MA.

[52] We have stated in section 4 (see also A. J. Ridley and G. Toth (unpublished data, 2008)) that the current I_{total} and ionospheric voltage $\Delta\varphi_{pc}$ are too low in the simulations owing to finite grid–resolution problems. Since the ratio $I_{total}/\Sigma_P\Delta\varphi_{pc}$ = W/L does not vary with grid resolution (see Figure 6), the ratio $I_{total}/\Delta\varphi_{pc} = W/L\Sigma_P = R_B$ does not vary with grid resolution. Hence, the value R_B = 0.0733Ω is not in error owing to the finite grid resolution. Examining expression (5), it is clear that since I_{total} is underestimated by the simulations, V_B is underestimated. Hence, if higher-resolution near-Earth region grids could be utilized, a value of V_B greater than 257 kV would be obtained. It also follows that if V_B is underestimated, then I_{max} = 3.5 MA is underestimated by the same fractional amount.

Table 6. Parameters Needed to Analyze the Solar Wind/Ionosphere Circuit for the High-Resolution Simulations

Case	Σ_P (mho)	R_{load} (Ω)	I (MA)
1	5	0.057	1.83
2	20	0.0143	2.84

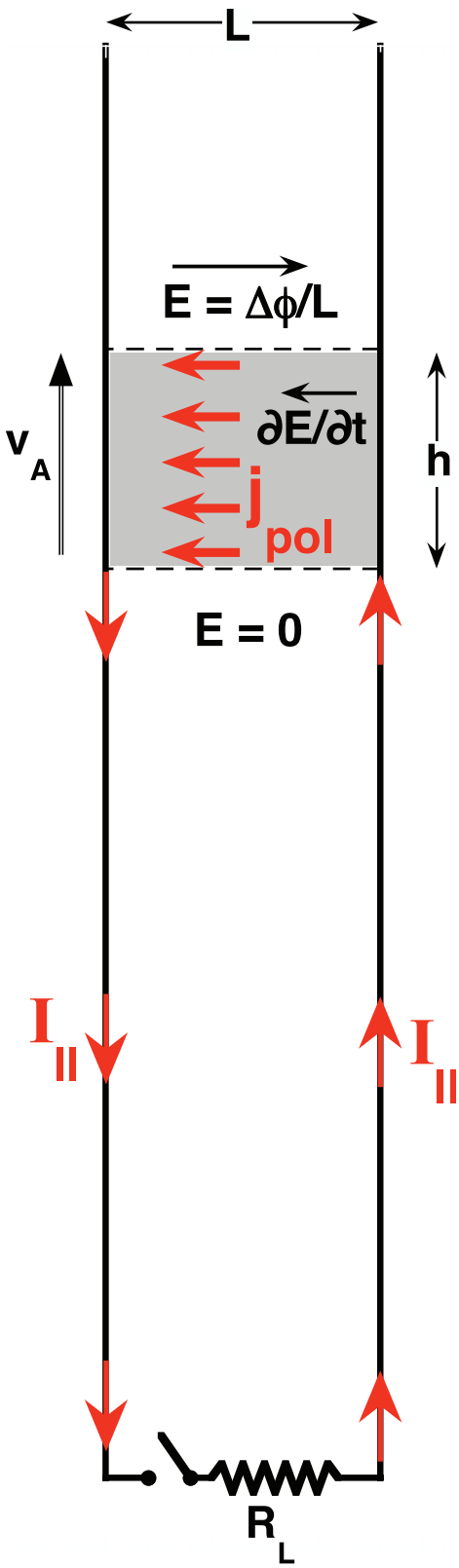

Figure 23. A sketch of the solar wind generator connected to ionospheric load. Connecting the load launches an upward traveling signal (gray region) that moves at the Alfven speed. The changing perpendicular electric field in the gray signal region produces a polarization drift current (red arrows) that feed field aligned currents into the ionosphere (red arrows).

[53] Finally, comparing the values of R_L in Table 6 with the value obtained for R_B (0.0733Ω), R_L was always less than R_B in the simulations. Hence the polar cap was always in some degree of saturation. For Σ_P = 5 mho, R_L was 9/10 of R_B (modest saturation) and for Σ_P = 20 mho R_L was less than 1/4 of R_B (strong saturation).

6.4. Circuit and the Physical World

[54] The values obtained via the circuit analysis of section 6.3 (V_B = 257 kV, $R_L = 0.33/\Sigma_P$, R_B = 0.0733Ω, and $I_{max} = V_B/R_B$ = 3.5 MA) make sense for the solar wind–driven magnetosphere. For the solar wind parameters of the simulations (v = 300 km s^{-1} and B_z = −10 nT), a potential of 257 kV corresponds to tapping a distance of 12.2 R_E across the solar wind motional generator, which is less than the diameter of the magnetosphere. This voltage value thus seems reasonable. It is, however, 15–75% higher than the values of $\Delta\varphi_{mag}$ measured in the simulations (see Table 2). The value $R_L = 0.33/\Sigma_P$ that was obtained in the analysis is what one gets for the definition of the ionospheric resistivity $L/W\Sigma_P$, which is the length L of the current path in the ionosphere divided by the Pedersen conductivity σ_P times the area. In section 3 it was found that the effective value of W/L is W/L = 3.0.

[55] Note that the BATSRUS simulation code obtains a Region-2 current which is very weak compared with an improved simulation code of BATSRUS combined with an inner-magnetospheric simulation model [*De Zeeuw et al.*, 2004]. The addition of a realistic Region-2 current could alter the value of R_L, which would change the value of I_{max}.

[56] In the following two paragraphs, two methods will be used to estimate the values of I_{max} and R_B for comparison with the circuit values I_{max} = 3.5 MA and R_B = 0.073 Ω: the Alfven conductance picture [cf. *Ridley*, 2007; *Kivelson and Ridley*, 2008] and the ram pressure picture [cf. *Siscoe et al.*, 2002b].

[57] The circuit values of I_{max} and R_B agree with an Alfven conductance picture of the generator [e.g., *Ridley*, 2007; *Kivelson and Ridley*, 2008]. In this picture I_{max} and R_B are calculated as follows. I_{max} is the maximum current that will flow from the solar wind generator, which would occur if a load with R_L = 0 were connected. Such a connection is sketched in Figure 23, with the ionosphere at the bottom, the solar wind at the top, and two vertical magnetic field lines connecting the ionosphere into the solar wind plasma. If the switch at the bottom is open (no load), then a potential $\Delta\varphi$ would exist at all heights between the two vertical field lines, where $\Delta\varphi = E_{sw}L$, with E_{sw} being the solar wind electric field vB/c and L being the distance between the two field lines. When the switch is closed (with R_L = 0), the potential across the field lines at the ionosphere is shorted out and this launches a discharge signal vertically up the "transmission line." This signal propagates at the local Alfven speed v_A [*Goertz and Boswell*, 1979]. The propagating signal is shown in Figure 23 as the gray patch, propagating upward at a speed v_A. Ahead of the signal the perpendicular electric field is undisturbed at $E_\perp = \Delta\varphi/L$, and behind the signal the electric field is $E_\perp$ = 0. (Above the gray patch in Figure 23 the direction of $E_\perp$ is noted with a black arrow.) Hence, as the signal propagates upward over a parcel of solar wind plasma, the plasma experiences a time changing electric field perpendicular to the magnetic field

$\partial E_\perp/\partial t$. The direction of $\partial E_\perp/\partial t$ is noted as the black arrow in the gray region in Figure 23. This $\partial E_\perp/\partial t$ leads to a polarization drift of the ions and electrons in the plasma in the opposite directions, dominated by the ions, which produces a current in the direction of $\partial E_\perp/\partial t$ perpendicular to *B*. The polarization-drift current is expressed as $j_{pol} = nm_i c^2/B^2\ \partial E_\perp/\partial t$ [*Nicholson*, 1983] and is sketched as the red arrows in the gray region of Figure 23. The quantity $\partial E_\perp/\partial t$ can be written $\Delta E/\Delta t$, where $\Delta E = (E_{sw} - 0) = \Delta\varphi/L$, and $\Delta t = h/v_A$, where h is the spatial extent of the signal along the direction of the magnetic field (see label in Figure 23). The value of h is governed by how rapidly the load is connected to the generator and it will soon drop out of the calculation. The current I_{max} that flows along the magnetic field to the ionosphere is the current density flowing perpendicular to the magnetic field in the gray region times the height h (along *B*) and width W (into the page) of the gray region. Thus $I_{max} = j_{pol}hW$. Using the above expression for j_{pol} with $\Delta E = \Delta\varphi/L$ and $\Delta t = h/v_A$ in it, and using $v_A = B/(4\pi nm_i)^{1/2}$, the expression $I_{max} = j_{pol}hW$ becomes

$$I_{max} = (W/L)c^2\Delta\varphi/4\pi v_A \tag{8}$$

(cf. equations (12) and (13) of *Borovsky* [1987]). For $\Delta\varphi = V_B = 257$ kV, $v_A = 156$ km s^{-1} (see Table 1), and W/L = 3.0, expression (8) yields $I_{max} = 3.93$ MA, which is close to the value of the 3.5 MA obtained from the analysis of the simulations using the circuit of Figure 22. The Alfven conductance picture of the generator yields a value of the internal resistance R_B of the generator as $R_B = \Delta\varphi/I_{max}$; using expression (8) for I_{max} this is

$$R_B = (L/W)4\pi v_A/c^2. \tag{9}$$

[58] Evaluating expression (9) with W/L = 3.0 and $v_A = 156$ km s^{-1} yields $R_B = 0.065\ \Omega$, which is close to the value of 0.073 Ω obtained from the analysis of the simulations using the circuit of Figure 22.

[59] The circuit values of I_{max} and R_B are in lesser agreement with the ram pressure picture of the generator. Using *Siscoe et al.*'s [2002b] prescription to estimate the maximum current I_{max} that can be driven onto the ionosphere by the ram pressure of the solar wind, the expression

$$I_{max} = 1.06\,\mathrm{MA}\,P_{sw}^{1/3} \tag{10}$$

is obtained, where P_{sw} is the solar wind pressure expressed in units of nPa. Expression (10) comes about by assuming that the total drag force on the magnetosphere is $F_{drag} = P_{sw}r^2$, where r is the magnetopause standoff distance given by $r = R_E(B_o/B_{pause})^2$, where B_o is the equatorial field strength at the Earth's surface and where the magnetopause magnetic field strength B_{pause} is given by pressure balance with the solar wind $B_{pause} = (8\pi P_{sw})^{1/2}$, and where the drag force is produced by a magnetic force on the magnetopause current $F_{drag} = rI_{max}B_{pause}/c$. In the previous sentence, there were four equations and four unknowns (I_{max}, r, B_{pause}, and F_{drag}), allowing expression (10) to be algebraically derived. For the present simulations $P_{sw} = 0.3$ nPa (see Table 1): using this value, expression (10) yields $I_{max} = 0.71$ MA. This estimate (which must be shared between the northern and southern polar caps) is considerably less than the $I_{max} = 3.5$ MA of the circuit. Before it can be discerned whether the parameters of the circuit of Figure 22 are consistent with the ram pressure–limiting picture, a better calculation of I_{max} owed to ram pressure of the solar wind must be made. (1) Taking a more accurate estimate of the cross-sectional area A of the magnetosphere ($A = r^2$ was used in the drag-force expression above) would increase the I_{max} estimate, (2) using a drag coefficient C_D [cf. *Hoerner*, 1965] in the drag-force expression $F_{drag} = C_D\,P_{sw}\,A$ could either increase or decrease the I_{max} estimate, (3) utilizing only the currents of the high-latitude magnetopause would decrease the I_{max} estimate, and (4) dividing the magnetopause current equally to the northern and southern ionospheres would halve the I_{max} estimate. The coefficient of drag for the low-β magnetosheath flow [*Lavraud et al.*, 2007] around the magnetosphere will be difficult to obtain. Note: in Appendix A the high-latitude magnetopause currents will be integrated in the simulations and will be found to be considerably smaller than the Region-1 currents flowing into the polar cap.

[60] According to this circuit picture and circuit interpretation, polar cap saturation means that $R_L \ll R_B$. In that case the voltage applied to the ionosphere is much less than V_B and the current flowing is near its maximum value V_B/R_B. In the present simulations, polar cap saturation was explored by varying R_L which varied the ratio R_L/R_B. Polar cap saturation could also be explored by varying R_B to vary the ratio R_L/R_B. The value of R_B can be varied by varying the Alfven speed of the solar wind (see expression (9)). For example, to vary $Q = v_A\Sigma_P/806$ (expression (2)), the present paper varies Σ_P, but one could also vary v_A. Note, according to this circuit analysis, one cannot get saturation by varying V_B while R_B and R_L are fixed. This could be attempted by varying the solar wind electric field E = vB/c by varying v and keeping B fixed (which keeps v_A fixed).

7. Summary of Findings

[61] Global MHD simulations with a high-resolution grid covering the dayside magnetopause were run with constant and ideal solar wind conditions. A resistive spot was placed on the dayside magnetopause to ensure that MHD captured the correct reconnection rate. The conductivity of the polar cap was varied and the simulations were analyzed. The main findings of the analysis are summarized below and some of them are collected into Table 4.

[62] 1. The potential $\Delta\varphi_{pc}$ measured across the polar cap in the ionosphere is reduced when the ionospheric Pedersen conductivity Σ_P increases with the solar wind parameters staying the same. In going from a Q value of 0.97 to a Q value of 3.9 (the range of mildly saturated to heavily saturated) the polar cap potential changes approximately according to the predicted $(1 + Q)^{-1}$ dependence, where $Q = v_A\Sigma_P/806$.

[63] 2. When the ionospheric Pedersen conductivity Σ_P increases, the Y component electric field E_y above the polar cap reduces. This corresponds to a mapping of the reduced polar cap potential $\Delta\varphi_{pc}$ along the magnetic field lines into the magnetospheric lobe.

[64] 3. When the ionospheric Pedersen conductivity Σ_P increases, the plasma flow velocity $v_\perp$ (and the field line

convection velocity) above the polar cap reduce. This corresponds to a mapping of the reduced polar cap potential $\Delta\varphi_{pc}$ along the magnetic field lines into the magnetospheric lobe.

[65] 4. The cross–polar cap current I_{total} increases modestly (by about 50%) when the ionospheric conductivity Σ_P is increased by a factor of 4. This is a Region-1 sense current flowing into the ionosphere on the dusk side, out of the ionosphere on the dawn side, and flowing dawn-to-dusk across the polar cap.

[66] 5. The geometrical factor $I_{total}/\Sigma_P\Delta\varphi_{pc}$ does not vary as the ionospheric conductivity Σ_P changes by a factor of 4, the polar cap potential $\Delta\varphi_{pc}$ changes by a factor of 2.5, and the polar cap current I_{total} changes by a factor of 1.5. The geometrical factor (dimensionless) is the ratio of the effective width of the current in the noon-midnight direction divided by the effective length of the cross–polar cap current in the dawn-dusk direction.

[67] 6. The local reconnection rate R at the dayside magnetosphere does not change as the ionospheric conductivity Σ_P changes and the polar cap potential $\Delta\varphi_{pc}$ is strongly reduced. The local reconnection rate is governed by the values of the local plasma parameters in the magnetosphere and the magnetosheath on either side of the magnetopause and these parameters do not change. This behavior is as expected from theoretical arguments [*Borovsky and Hesse*, 2007; *Cassak and Shay*, 2007; *Borovsky*, 2008].

[68] 7. The cross-magnetosphere potential $\Delta\varphi_{mag}$ does not show a systematic change as the ionospheric conductivity Σ_P and the polar cap potential $\Delta\varphi_{pc}$ both strongly change. The cross-magnetosphere potential $\Delta\varphi_{mag}$ is a measure of the total rate of reconnection on the dayside magnetopause.

[69] 8. The magnetic field strength B in the dayside magnetosphere weakens when the ionospheric Pedersen conductivity Σ_P increases. There are no changes in the solar wind parameters in the simulations; this weakening of B is attributed to the magnetic perturbation caused by the cross–polar cap current I_{total}.

[70] 9. The magnetopause at the nose of the magnetosphere moves inward when the ionospheric Pedersen conductivity Σ_P increases. This movement closer to the Earth is attributed to the ram pressure of the solar wind being balanced by a weakened magnetic field of the dayside magnetosphere.

[71] 10. The magnetic field strength at the dayside magnetopause does not change when the ionospheric Pedersen conductivity Σ_P increases and the polar cap potential $\Delta\varphi_{pc}$ reduces. This field strength at the magnetopause is determined by the pressure of the solar wind, and this constancy of the field strength is consistent with the observed constancy of the dayside reconnection rate.

[72] 11. The flaring of the magnetosphere at the terminator does not change significantly as the ionospheric Pedersen conductivity Σ_P increases substantially and the polar cap potential $\Delta\varphi_{pc}$ reduces substantially. This flaring is quantified as the distance from the Earth to the magnetopause at the terminator.

[73] 12. X component magnetic perturbations B_x appear over the polar caps and strengthen as the ionospheric Pedersen conductivity Σ_P increases. This perturbation is in part owed to the cross–polar cap current I_{total}.

[74] 13. The cusps of the magnetosphere shift equatorward as the ionospheric Pedersen conductivity Σ_P increases. This may be associated with the weakening of the magnetic field strength in the dayside magnetosphere with increasing Pedersen conductivity.

[75] 14. The closed field line region of the dayside magnetosphere flattens in the Z direction as the ionospheric Pedersen conductivity Σ_P increases and the polar cap potential $\Delta\varphi_{pc}$ reduces. This flattening may be related to the weakening of the magnetic field strength on the dayside as the Pedersen conductivity increases.

[76] 15. When the spatial resolution of the near-Earth region and above-the-polar cap regions is increased, the polar cap potential $\Delta\varphi_{pc}$ increases and the cross–polar cap current I_{total} increases, but the local reconnection rate R at the dayside magnetopause and the cross-magnetosphere potential $\Delta\varphi_{mag}$ do not change.

[77] 16. A circuit analysis of the polar cap saturation phenomena measured in the simulations based on the solar wind being a current-limited voltage generator reproduces the behavior quite well and yields reasonable values for the voltage source and the current limit.

Appendix A

A1. Relation to Polar Cap Saturation Models

[78] In Appendix A nine explanations for polar cap saturation in the literature are collected and these nine models are discussed relative to the findings of the present study. (See also *Siscoe et al.* [2004], *Shepherd* [2007], and *Lavraud and Borovsky* [2008] for reviews of the various models.) The polar cap saturation models can be separated into "reconnection models" and "postreconnection models." The reconnection models (models 1–6 below) explain the reduction of the polar cap potential via a reduction in the reconnection rate at the dayside magnetosphere, i.e., by a reduction of solar wind/magnetosphere coupling. The postreconnection models explain the reduction of the polar cap potential by physical processes happening after the solar wind plasma reconnects with the magnetosphere.

[79] In the discussions below, particular attention is paid to whether or not the present findings support the various models. Note, however, that just because contradictions are found between the findings of the present paper and the various models does not mean that those models can't explain the occurrence of polar cap saturation under different circumstances than were explored here, for instance under super strong driving. Also, global MHD codes are not the real magnetosphere and simulation results need to be checked against spacecraft measurements. A summary of this assessment appears in Table A1.

A1.1. Hill Model

[80] In the Hill model [*Hill et al.*, 1976; *Siscoe et al.*, 2002a] it is argued that the strong dawn-to-dusk cross–polar cap currents reduce the magnetic field strength in the dayside magnetosphere and at the dayside reconnection site. In the model, this reduction of the field strength at the reconnection site lowers the Alfven speed there, and therefore lowers the rate of reconnection. This lowered rate of reconnection at the dayside reduces solar wind/magneto-

Table A1. Nine Models for Polar Cap Saturation From the Literature Assessed as to Whether or Not the Present Findings Contradict the Explanation

"Model"	Explanation	References	Present Analysis Contradicts	No Contradictions Found
Hill model	Weakened dayside field reduces reconnection rate	*Hill et al.* [1976] and *Siscoe et al.* [2002a]	yes	
Flaring model	Flaring reduces reconnection rate	*Merkin et al.* [2005a, 2005b]	yes	
X-line-length model	Changes in size of magnetosphere reduces total reconnection	*Raeder and Lu* [2005] and *Ridley* [2005]	yes	
Magnetosheath flow model	Changes in solar wind conditions change dayside reconnection rate	*Pudovkin et al.* [1985] and *Ridley* [2005]	yes	
Lobe-bulge model	Bulging lobes hinders dayside reconnection	*Raeder et al.* [2001]	yes	
Bow shock model	Polar cap currents modify bow shock and dayside reconnection rate.	*Hernandez et al.* [2007]	yes	
Ionospheric-outflow model	Mass loading of magnetospheric convection by ionospheric outflow	*Winglee et al.* [2002]	yes	
Ram pressure–saturation model	Ram pressure limits currents	*Siscoe et al.* [2002b]	yes	
MHD generator model	Solar wind MHD generator is loaded down	*Ridley* [2007] and *Kivelson and Ridley* [2008]		yes

sphere coupling and is the cause of the polar cap saturation. The present findings contradict this explanation. Whereas the magnetic field strength of the dayside magnetosphere *is* reduced by the cross–polar cap currents, the magnetic field strength at the dayside magnetopause is determined by pressure balance with the solar wind and hence is not reduced by the currents. Further, the measured reconnection rate in the present simulations does not change as the magnitude of the cross–polar cap currents change.

A1.2. Flaring Model

[81] In the flaring model [*Merkin et al.*, 2005a, 2005b] the change of shape of the dayside magnetopause changes the flow of the magnetosheath around the Earth and reduces the total amount of reconnection between the solar wind and the magnetosphere. In particular, a strengthening of the cross–polar cap currents causes the distance to the magnetopause at the terminators to increase, increasing the flaring of the magnetosphere. The present findings contradict this explanation in two manners. First, the distance to the magnetopause at the terminator does not change substantially as the polar cap potential $\Delta\varphi_{pc}$ changes substantially and the cross–polar cap currents I_{total} change substantially. Second, the total amount of reconnection as measured by the cross-magnetosphere potential $\Delta\varphi_{mag}$ does not change significantly as the cross–polar cap potential $\Delta\varphi_{pc}$ changes significantly.

A1.3. X-Line-Length Model

[82] In the X-line-length model [*Raeder and Lu*, 2005; *Ridley*, 2005] [see also *Pudovkin et al.*, 1985] changes in solar wind parameters result in changes in the size of the magnetosphere, which changes the length of the dayside reconnection line, which can reduce the total amount of reconnection between the solar wind and the magnetosphere to cause polar cap saturation. The present findings contradict this explanation in two manners. First, the cross–polar cap potential $\Delta\varphi_{pc}$ changes significantly without a change in the solar wind conditions and without an appreciable change in the size of the magnetosphere. Second, the total amount of reconnection as measured by the cross-magnetosphere potential $\Delta\varphi_{mag}$ does not change significantly as the cross–polar cap potential $\Delta\varphi_{pc}$ changes significantly.

A1.4. Magnetosheath-Flow Model

[83] In the magnetosheath-flow model [*Pudovkin et al.*, 1985; *Ridley*, 2005] variations in the solar wind parameters produce variations in the properties of the magnetosheath flow that change the total reconnection rate between the solar wind and the magnetosphere, which can lead to polar cap saturation. *Pudovkin et al.* [1985] considers changes in the length of the flow stagnation line with changes in the solar wind; *Ridley* [2005] considers changes in the magnetosheath electric field with changes in the solar wind. The present findings contradict this explanation in two manners. First, the cross–polar cap potential $\Delta\varphi_{pc}$ changes significantly without a change in the solar wind conditions. Second, the total amount of reconnection as measured by the cross-magnetosphere potential $\Delta\varphi_{mag}$ does not change significantly as the cross–polar cap potential $\Delta\varphi_{pc}$ changes significantly.

A1.5. Lobe-Bulge Model

[84] In this model [*Raeder et al.*, 2001] [see also *Maynard et al.*, 2004; *Ober et al.*, 2006], referred to as the "dimple model" by *Siscoe et al.* [2004], the cross–polar cap currents weaken the dayside magnetic field strength allowing the lobes (region of open field lines from the polar cap) to bulge forward into the magnetosheath flow, creating a stagnation flow in the magnetosheath in front of the dayside neutral line which lowers the reconnection rate between the solar wind and magnetosphere, which can lead to polar cap saturation. The present findings contradict this explanation in two manners. First, polar cap saturation is found to occur

Figure A1. The plasma density of the magnetosphere is explored with two snapshots from the simulation in Figure 2. (a, c, e) From a time (t = 65 min) when $\Sigma_P = 5$ mho with modest saturation ($\Delta\varphi_{pc} = 65.6$ kV) and (b, d, f) from a time (t = 120 min) when $\Sigma_P = 20$ mho with strong saturation ($\Delta\varphi_{pc} = 20.3$ kV). Figures A1a and A1b show the plasma number density in the X = 0 plane, Figures A1c and A1d show the plasma number density in the Z = 0 plane, and Figures A1e and A1f show the plasma number density in the Y = 0 plane.

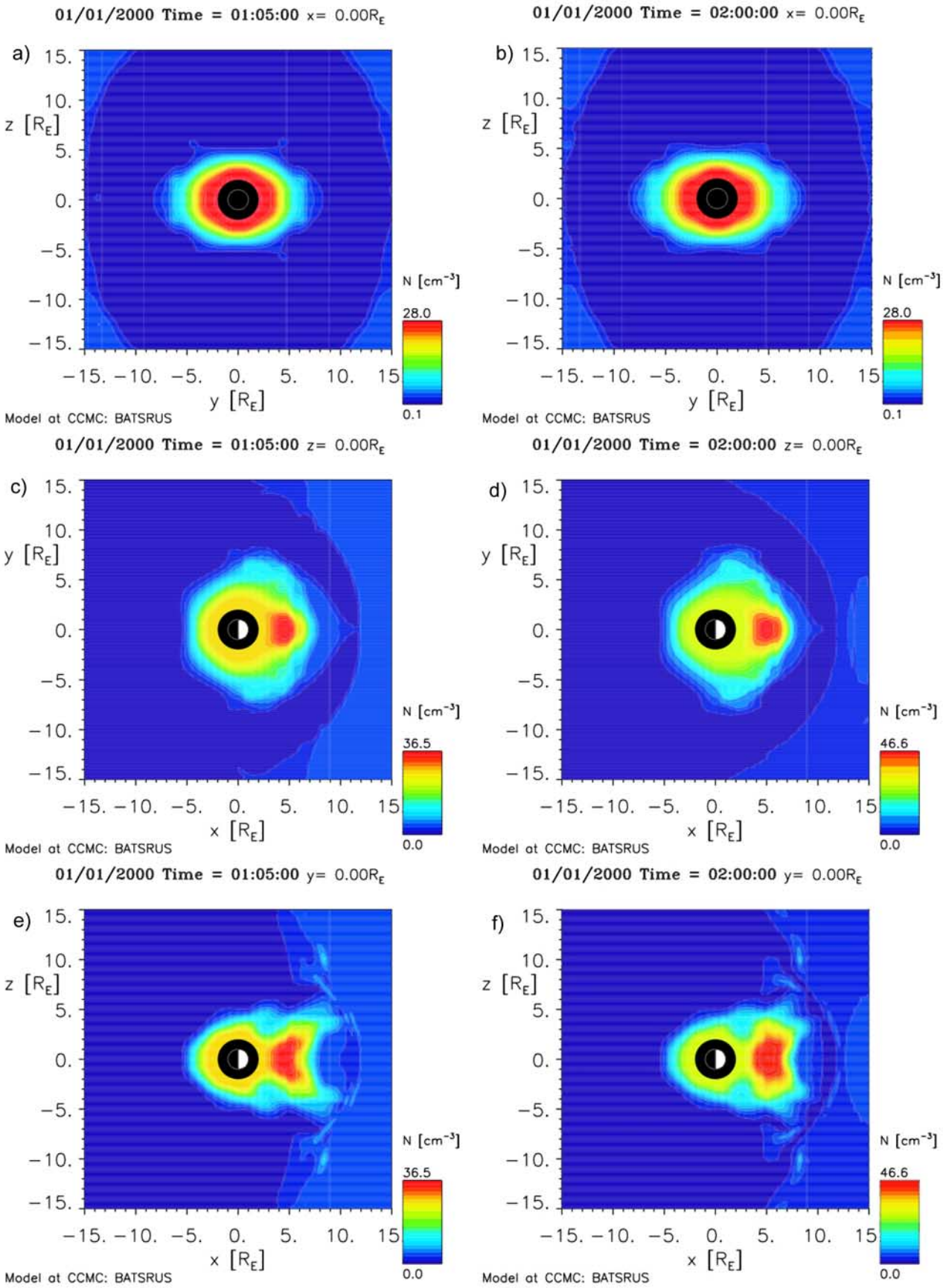
01/01/2000 Time = 01:05:00 x= 0.00R_E
a)
z [R_E]
y [R_E]
N [cm^-3]
28.0
0.1
Model at CCMC: BATSRUS
01/01/2000 Time = 02:00:00 x= 0.00R_E
b)
z [R_E]
y [R_E]
N [cm^-3]
28.0
0.1
Model at CCMC: BATSRUS
01/01/2000 Time = 01:05:00 z= 0.00R_E
c)
y [R_E]
x [R_E]
N [cm^-3]
36.5
0.0
Model at CCMC: BATSRUS
01/01/2000 Time = 02:00:00 z= 0.00R_E
d)
y [R_E]
x [R_E]
N [cm^-3]
46.6
0.0
Model at CCMC: BATSRUS
01/01/2000 Time = 01:05:00 y= 0.00R_E
e)
z [R_E]
x [R_E]
N [cm^-3]
36.5
0.0
Model at CCMC: BATSRUS
01/01/2000 Time = 02:00:00 y= 0.00R_E
f)
z [R_E]
x [R_E]
N [cm^-3]
46.6
0.0
Model at CCMC: BATSRUS

Figure A1

Table A2. Integrated Region-1 Currents Into the Northern Polar Cap Compared With Integrated Current at the Northern High-Latitude Magnetopause[a]

Case	Σ_P (mho)	I_{total} (MA)	$I_{magnetopause}$ (MA)
1	5	1.84	0.91
2	20	2.83	0.70

[a]Both cases use high-resolution near-Earth regions, and both have the same solar wind parameters (v = 300 km s^{-1}, B_z = −10 nT, and n = 2 cm^{-3}).

in a regime where lobe bulge does not severely affect the flow of the magnetosheath. Second, polar cap saturation is found to occur without the reconnection rate at the dayside being reduced.

A1.6. Bow Shock Model

[85] In this model [*Hernandez et al.*, 2007] the currents flowing from the polar cap connect across the bow shock, modifying the shock properties, and the modified bow shock in turn modifies the properties of the magnetosheath, changing the electric field at the magnetopause to change the reconnection rate, which can lead to polar cap saturation. The present findings contradict this explanation. The polar cap potential $\Delta\varphi_{pc}$ is observed to change without any changes in the dayside reconnection rate.

A1.7. Ionospheric-Outflow Model

[86] In this model [*Winglee et al.*, 2002] an increase of driving of the magnetosphere by the solar wind causes an increase in the ionospheric-plasma outflow into the magnetosphere and this plasma mass loads magnetosphere convection, which reduces the potential of the magnetosphere and the ionosphere. The present findings contradict this explanation of polar cap saturation in two manners. First, polar cap saturation is observed without any change in the parameters of the solar wind. Second, the cross–polar cap potential $\Delta\varphi_{pc}$ changes significantly without an appreciable change in the plasma mass density in the magnetosphere. This latter point is demonstrated in Figure A1, where the plasma number density in a weakly saturated case ($\Delta\varphi_{pc}$ = 65.6 kV: left column) is compared with the plasma number density in a strongly saturated case ($\Delta\varphi_{pc}$ = 20.3 kV: right column). In Figures A1a and A1b the density is shown in the Y = 0 plane (terminator plane), in Figures A1c and A1d the density is shown in the Z = 0 plane (equatorial plane), and in Figures A1e and A1f the density is shown in the Y = 0 plane (noon-midnight meridianal plane). The color scales between Figures A1a, A1c, and A1e and Figures A1b, A1d, and A1f differ by only 20% or less. It is safe to conclude that there is not sufficiently more mass loading of magnetospheric convection in the right column than there is in the left column to reduce the convection of the left column down to 20.3/65.6 = 31% of its value.

A1.8. Ram Pressure–Saturation Model

[87] In this model [*Siscoe et al.*, 2002b] the cross–polar cap current is limited by the amount of momentum that the solar wind flow carries, which limits the amount of $j \times \underline{B}$-generated current that the solar wind can drive into the Earth's ionosphere. The present findings provide mixed support for this explanation. The finding that the cross–polar cap current I_{total} does not change significantly as Σ_P and $\Delta\varphi_{pc}$ undergo large changes implies that the current I_{total} is being driven by a generator that is current limited, which provides some support for this model. However, the estimates of the current at the magnetopause fall short of the maximum current in the circuit analysis of the simulations. This is tested by integrating the high-latitude magnetopause current in the simulations and comparing this current with the cross–polar cap current in the simulations. For the northern high-latitude magnetopause and the northern polar cap, these values appear in Table A2 for a weakly saturated simulation (Σ_P = 5 mho) and for a strongly saturated simulation (Σ_P = 20 mho), both with high-resolution near-Earth regions and both with the same solar wind parameters. The high-latitude current integration is of j_y passing through the Y = 0 plane. Since the dawn-to-dusk current of the polar cap flows in the +Y direction, only regions of $j_y < 0$ are integrated in the magnetopause region. As can be seen in Table A2, the currents in the vicinity of the high-latitude magnetopause are insufficient by factors of 2 to 4 to account for the cross–polar cap current. Tracing electrical current flow lines in the simulations finds that some of the cross–polar cap current closes near the high-latitude magnetopause, particularly when low- and medium-resolution near-Earth regions are used; this tracing provides some support for the ram pressure–saturation model. (The authors have been cautioned (J. Birn, private communication, 2007) that tracing current lines does not necessarily connect a generator to a load and does not necessarily identify cause and effect.)

A1.9. MHD-Generator Model

[88] In this model [*Ridley*, 2007; *Kivelson and Ridley*, 2008] the motion of the reconnected solar wind (magnetosheath) plasma past the Earth acts as an MHD generator transferring its motional potential to the ionosphere by means of field-aligned currents, which are limited in strength by the "Alfven conductance" of the solar wind plasma. (The MHD-generator model and the ram pressure–saturation model have much in common: the total amount of current supplied by the Alfven conductance limit is equal to the amount of current needed to $j \times \underline{B}$ brake the momentum of the plasma flow [*Borovsky*, 1987].) The present findings do not contradict this MHD-generator explanation. The finding that the cross–polar cap current I_{total} does not change significantly as Σ_P and $\Delta\varphi_{pc}$ make large changes implies that the current I_{total} is being driven by a generator that is current limited, which provides some support for this model, as it did for the ram-current–saturation model. And, the circuit analysis of the simulations in section 6.4 yields a value for the current limit that is consistent with concepts of the MHD-generator model. Further, tracing electrical current flow lines in the simulations finds that some of the cross–polar cap current closes in the distant lobe far from the Earth, particularly at high resolutions of the near-Earth regions. This tracing provides further support for the MHD-generator model.

[89] **Acknowledgments.** The authors wish to thank Joachim Birn, Aaron Ridley, and Howard Singer for helpful conversations. All simulations were performed using the Community Coordinated Modeling Center (CCMC) at Goddard Space Flight Center using the BATSRUS Model. The CCMC is a multiagency partnership between NASA, NSF, AFMC,

AFOSR, AFRL, AFWA, NOAA, and ONR. The BATSRUS Model was developed by the Center for Space Environment Modeling at the University of Michigan. Joe Borovsky would also like to acknowledge the CCMC at NASA/Goddard Space Flight Center for their hospitality. This work was supported by the NSF National Space Weather Program (at Los Alamos) and by the Los Alamos LDRD Program.

[90] Amitava Bhattacharjee thanks C. Clauer and Daniel Weimer for their assistance in evaluating this paper.

References

Alfven, H., and C.-G. Falthammar (1963), *Cosmical Electrodynamics*, sect. 5.3, Oxford at the Clarendon Press, London.

Axford, W. I. (1964), Viscous interaction between the solar wind and the Earth's magnetosphere, *Planet. Space Sci.*, *12*, 45–53, doi:10.1016/0032-0633(64)90067-4.

Bellaire, P. J. (2004), Space weather research in the US Air Force Office of Scientific Research, in *Effects of Space Weather on Technology Infrastructure*, edited by I. A. Daglis, pp. 319–330, Kluwer Acad., Dordrecht, Netherlands.

Birn, J. (1989), Three-dimensional equilibria for the extended magnetotail and the generation of field-aligned current sheets, *J. Geophys. Res.*, *94*, 252–260.

Birn, J., and M. Hesse (2001), Geospace Environment Modeling (GEM) magnetic reconnection challenge: Resistive tearing, anisotropic pressure and Hall effects, *J. Geophys. Res.*, *106*, 3737–3750, doi:10.1029/1999JA001001.

Birn, J., and M. Hesse (2007), Reconnection rates in driven magnetic reconnection, *Phys. Plasmas*, *14*, 082306, doi:10.1063/1.2752510.

Birn, J., et al. (2001), Geospace Environment Modeling (GEM) Magnetic Reconnection Challenge, *J. Geophys. Res.*, *106*, 3715–3719, doi:10.1029/1999JA900449.

Birn, J., J. E. Borovsky, and M. Hesse (2008), Properties of asymmetric magnetic reconnection, *Phys. Plasmas*, *15*, 1.

Borovsky, J. E. (1987), Limits on the cross-field propagation of streams of cold plasma, *Phys. Fluids*, *30*, 2518, doi:10.1063/1.866090.

Borovsky, J. (2004), Global sawtooth oscillations of the magnetosphere, *Eos Trans. AGU*, *85*(49), doi:10.1029/2004EO490009.

Borovsky, J. E. (2008), The rudiments of a theory of solar wind/magnetosphere coupling derived from first principles, *J. Geophys. Res.*, *113*, A08228, doi:10.1029/2007JA012646.

Borovsky, J. E., and M. H. Denton (2006a), The differences between CME-driven storms and CIR-driven storms, *J. Geophys. Res.*, *111*, A07S08, doi:10.1029/2005JA011447.

Borovsky, J. E., and M. H. Denton (2006b), The effect of plasmaspheric drainage plumes on solar-wind/magnetosphere coupling, *Geophys. Res. Lett.*, *33*, L20101, doi:10.1029/2006GL026519.

Borovsky, J. E., and M. Hesse (2007), The reconnection of magnetic fields between plasmas with different densities: Scaling relations, *Phys. Plasmas*, *14*, 102309, doi:10.1063/1.2772619.

Borovsky, J. E., and J. T. Steinberg (2006), The "calm before the storm" in CIR/magnetosphere interactions: Occurrence statistics, solar-wind statistics, and magnetospheric preconditioning, *J. Geophys. Res.*, *111*, A07S10, doi:10.1029/2005JA011397.

Borovsky, J. E., J. Birn, and A. J. Ridley (2004), BATSRUS/CCMC simulations of the magnetosphere for the solar-wind conditions that drive global sawtooth oscillations, *Eos Trans. AGU*, *85*(17), Spring Meet. Suppl., Abstract SM12B–06.

Borovsky, J. E., M. Hesse, J. Birn, and M. M. Kuznetsova (2008), What determines the reconnection rate at the dayside magnetosphere?, *J. Geophys. Res.*, *113*, A07210, doi:10.1029/2007JA012645.

Bostrom, R. (1973), Electrodynamics of the ionosphere, in *Cosmical Geophysics*, edited by A. Egeland, Ø. Holter, and A. Omholt, pp. 181–192, Universitetsforlaget, Oslo.

Cahill, L. J., and P. G. Amazeen (1963), The boundary of the geomagnetic field, *J. Geophys. Res.*, *68*, 1835–1843.

Candidi, M., S. Orsini, M. Stokholm, and R. C. Elphic (1990), On the structure of the tail magnetic field, *J. Geophys. Res.*, *95*, 7929–7936, doi:10.1029/JA095iA06p07929.

Cassak, P. A., and M. A. Shay (2007), Scaling of asymmetric magnetic reconnection in collisional plasmas, *Phys. Plasmas*, *14*, 102144.

Clauer, C. R., F. Wilder, J. Baker, and M. Hairston (2007), Ionospheric convection during very weak IMF and solar wind driving, *Eos Trans. AGU*, *88*(52), Fall Meet. Suppl., Abstract SM13B–1321.

De Zeeuw, D. L., T. I. Gombosi, C. P. T. Groth, K. G. Powell, and Q. F. Stout (2000), An adaptive MHD method for global space weather simulations, *IEEE Trans. Plasma Sci.*, *28*, 1956–1965.

De Zeeuw, D. L., S. Sazykin, R. A. Wolf, T. I. Gombosi, A. J. Ridley, and G. Toth (2004), Coupling of a global MHD code and an inner magnetospheric model: Initial results, *J. Geophys. Res.*, *109*, A12219, doi:10.1029/2003JA010366.

Farrugia, C. J., A. Grocott, P. E. Sandholt, S. W. H. Cowley, Y. Miyoshi, F. J. Rich, V. K. Jordanova, R. B. Torbert, and A. Sharma (2007), The magnetosphere under weak solar wind forcing, *Ann. Geophys.*, *25*, 191.

Fedder, J. A., and J. G. Lyon (1987), The solar wind-magnetosphere-ionosphere current-voltage relationship, *Geophys. Res. Lett.*, *14*, 880–883, doi:10.1029/GL014i008p00880.

Floyd, L., J. Newmark, J. Cook, L. Herring, and D. McMullin (2005), Solar EUV and UV spectral irradiances and solar indices, *J. Atmos. Sol. Terr. Phys.*, *67*, 3–15, doi:10.1016/j.jastp.2004.07.013.

Goertz, C. K., and R. W. Boswell (1979), Magnetosphere-ionosphere coupling, *J. Geophys. Res.*, *84*, 7239–7246, doi:10.1029/JA084iA12p07239.

Gombosi, T. I., D. L. De Zeeuw, C. P. T. Groth, and K. G. Powell (2000), Magnetospheric configuration for Parker-spiral IMF conditions: Results of a 3D AMR MHD simulation, *Adv. Space Res.*, *26*, 139, doi:10.1016/S0273-1177(99)01040-6.

Goodman, M. L. (1995), A three-dimensional, iterative mapping procedure for the implementation of an ionosphere-magnetosphere anisotropic Ohm's law boundary condition in global magnetohydrodynamic simulations, *Ann. Geophys.*, *13*, 843, doi:10.1007/s00585-995-0843-z.

Gosling, J. T., D. N. Baker, S. J. Bame, W. C. Feldman, R. D. Zwickl, and E. J. Smith (1987), Bidirectional solar wind electron heat flux events, *J. Geophys. Res.*, *92*, 8519–8535, doi:10.1029/JA092iA08p08519.

Hairston, M. R., K. A. Drake, and R. Skoug (2005), Saturation of the ionospheric polar cap potential during the October–November 2003 superstorms, *J. Geophys. Res.*, *110*, A09S26, doi:10.1029/2004JA010864.

Hernandez, S., R. E. Lopez, M. Wiltberger, and J. G. Lyon (2007), MHD simulations of solar wind-geospace coupling, *Eos Trans. AGU*, *88*(23), Spring Meet. Suppl., Abstract SM51C–03.

Hill, T. W., A. Dessler, and R. A. Wolf (1976), Mercury and Mars: The role of ionospheric conductivity in the acceleration of magnetospheric particles, *Geophys. Res. Lett.*, *3*, 429–432, doi:10.1029/GL003i008p00429.

Hoerner, S. F. (1965), *Fluid-dynamic drag, report*, Hoerner Fluid Dyn., Brick Town, N. J.

Hones, E. W. (1963), Motions of charged particles trapped in the Earth's magnetosphere, *J. Geophys. Res.*, *68*, 1209–1219, doi:10.1029/JZ068i005p01209.

Iijima, T., and T. A. Potemra (1976), The amplitude distribution of field-aligned currents at northern high latitudes observed by Triad, *J. Geophys. Res.*, *81*, 2165–2174, doi:10.1029/JA081i013p02165.

King, J. H., and N. E. Papitashvili (2005), Solar wind spatial scales in and comparisons of hourly wind and ACE plasma and magnetic field data, *J. Geophys. Res.*, *110*, A02104, doi:10.1029/2004JA010649.

Kivelson, M. G., and A.J. Ridley (2008), Saturation of the polar cap potential: Inference from Alfvén wing arguments, *J. Geophys. Res.*, *113*, A05214, doi:10.1029/2007JA012302.

Lavraud, B., and J. E. Borovsky (2008), Altered solar wind-magnetosphere interaction at low Mach numbers: Coronal mass ejections, *J. Geophys. Res.*, *113*, A00B08, doi:10.1029/2008JA013192.

Lavraud, B., J. E. Borovsky, A. J. Ridley, E. W. Pogue, M. F. Thomsen, H. Reme, A. N. Fazakerley, and E. A. Lucek (2007), Strong bulk plasma acceleration in Earth's magnetosheath: A magnetic slingshot effect?, *Geophys. Res. Lett.*, *34*, L14102, doi:10.1029/2007GL030024.

Maynard, N. C., et al. (2004), Observed and simulated depletion layers with soutward IMF, *Ann. Geophys.*, *22*, 2151.

Merkin, V. G., A. S. Sharma, K. Papadopoulos, G. Milikh, J. Lyon, and C. Goodrich (2005a), Global MHD simulations of the strongly driven magnetosphere: Modeling of the transpolar potential saturation, *J. Geophys. Res.*, *110*, A09203, doi:10.1029/2004JA010993.

Merkin, V. G., A. S. Sharma, K. Papadopoulos, G. Milikh, J. Lyon, and C. Goodrich (2005b), Relationship between the ionospheric conductance, field aligned current, and magnetopause geometry: Global MHD simulations, *Planet. Space Sci.*, *53*, 873–879, doi:10.1016/j.pss.2005.04.001.

Merkine, V. G., K. Papadopoulos, G. Milikh, A. S. Sharma, X. Shao, J. Lyon, and C. Goodrich (2003), Effects of the solar wind electric field and ionospheric conductance on the cross polar cap potential: Results of global MHD modeling, *Geophys. Res. Lett.*, *30*(23), 2180, doi:10.1029/2003GL017903.

Mozer, F. S. (1984), Electric-field evidence on the viscous interaction at the magnetopause, *Geophys. Res. Lett.*, *11*, 135–138, doi:10.1029/GL011i002p00135.

Nicholson, D. R. (1983), *Introduction to Plasma Theory*, sect. 2.5, Wiley, New York.

Ober, D. M., N. C. Maynard, and W. J. Burke (2003), Testing the Hill model of transpolar potential saturation, *J. Geophys. Res.*, *108*(A12), 1467, doi:10.1029/2003JA010154.

Ober, D. M., N. C. Maynard, W. J. Burke, G. R. Wilson, and K. D. Siebert (2006), "Shoulders" on the high-latitude magnetopause: Polar/GOES

observations, *J. Geophys. Res.*, *111*, A10213, doi:10.1029/2006JA011799.

Powell, K., P. Roe, T. Linde, T. Gombosi, and D. L. De Zeeuw (1999), A solution-adaptive upwind scheme for ideal magnetohydrodynamics, *J. Comput. Phys.*, *154*, 284, doi:10.1006/jcph.1999.6299.

Pudovkin, M. I., S. A. Zaitseva, T. A. Bazhenova, and V. G. Andrezen (1985), Electric fields and currents in the Earth's polar caps, *Planet. Space Sci.*, *33*, 407–414, doi:10.1016/0032-0633(85)90085-6.

Raeder, J., and G. Lu (2005), Polar cap saturation during large geomagnetic storms, *Adv. Space Res.*, *36*, 1804.

Raeder, J., Y. L. Wang, and H. J. Singer (2001), Global simulation of magnetospheric space weather effects of the Bastille Day storm, *Sol. Phys.*, *204*, 323, doi:10.1023/A:1014228230714.

Reiff, P. H., and J. G. Luhmann (1986), Solar wind control of the polar-cap voltage, in *Solar Wind-Magnetosphere Coupling*, edited by Y. Kamide and J. A. Slavin, pp. 453–476, Terra Sci., Tokyo.

Reiff, P. H., R. W. Spiro, and T. W. Hill (1981), Dependence of polar cap potential drop on interplanetary parameters, *J. Geophys. Res.*, *86*, 7639–7648.

Ridley, A. J. (2005), A new formulation for the ionospheric cross polar cap potential including saturation effects, *Ann. Geophys.*, *23*, 3533.

Ridley, A. J. (2007), Alfven wings at Earth's magnetosphere under strong interplanetary magnetic fields, *Ann. Geophys.*, *25*, 533.

Ridley, A. J., T. I. Gombosi, and D. L. De Zeeuw (2004), Ionospheric control of the magnetosphere: Conductance, *Ann. Geophys.*, *22*, 567.

Ridley, A. J., D. L. De Zeeuw, W. B. Manchester, and K. C. Hansen (2006), The magnetospheric and ionospheric response to a very strong interplanetary shock and coronal mass ejection, *Adv. Space Res.*, *38*, 263, doi:10.1016/j.asr.2006.06.010.

Rufenach, C. L., R. F. Martin Jr., and H. H. Sauer (1989), A study of geosynchronous magnetopause crossings, *J. Geophys. Res.*, *94*, 15,125–15,134.

Russell, C. T., J. G. Luhmann, and G. Lu (2001), Nonlinear response of the polar ionosphere to large values of the interplanetary electric field, *J. Geophys. Res.*, *106*, 18,495–18,504, doi:10.1029/2001JA900053.

Sergeev, V. A., and B. M. Kuznetsov (1981), Quantitative dependence of the polar cap electric field on the IMF Bz-component and solar wind velocity, *Planet. Space Sci.*, *29*, 205–213, doi:10.1016/0032-0633(81)90034-9.

Shepherd, S. G. (2007), Polar cap potential saturation: Observations, theory, and modeling, *J. Atmos. Sol. Terr. Phys.*, *69*, 234–248, doi:10.1016/j.jastp.2006.07.022.

Siscoe, G. L., G. M. Erickson, B. U. O. Sonnerup, N. C. Maynard, J. A. Schoendorf, K. D. Siebert, D. R. Weimer, W. W. White, and G. R. Wilson (2002a), Hill model of transpolar potential saturation: Comparisons with MHD simulations, *J. Geophys. Res.*, *107*(A6), 1075, doi:10.1029/2001JA000109.

Siscoe, G. L., N. U. Crooker, and K. D. Siebert (2002b), Transpolar potential saturation: Roles of the region 1 current system and solar wind ram pressure, *J. Geophys. Res.*, *107*(A10), 1321, doi:10.1029/2001JA009176.

Siscoe, G., J. Rader, and A. J. Ridley (2004), Transpolar potential saturation models compared, *J. Geophys. Res.*, *109*, A09203, doi:10.1029/2003JA010318.

Sokolov, I. V., E. V. Timofeev, I. J.-Sakai, and K. Takayama (2002), Artificial wind — A new framework to construct simple and efficient upwind shock-capturing schemes, *J. Comput. Phys.*, *181*, 354, doi:10.1006/jcph.2002.7130.

Sonnerup, B. U. O., K. D. Siebert, W. W. White, D. R. Weimer, N. C. Maynard, J. A. Schoendorf, G. R. Wilson, G. L. Siscoe, and G. M. Erickson (2001), Simulations of the magnetosphere for zero interplanetary magnetic field: The ground state, *J. Geophys. Res.*, *106*, 29,419–29,434, doi:10.1029/2001JA000124.

Tsurutani, B. T., and W. D. Gonzalez (1995), The efficiency of "viscous interaction" between the solar wind and the magnetosphere during intense northward IMF events, *Geophys. Res. Lett.*, *22*, 663–666, doi:10.1029/95GL00205.

Ugai, M., and T. Tsuda (1977), Magnetic field-line reconnexion by localized enhancement of resistivity. Part 1, *J. Plasma Phys.*, *17*, 337.

Weimer, D. R. (1995), Models of high-latitude electric potentials derived with a least error fit of spherical harmonic coefficients, *J. Geophys. Res.*, *100*, 19,595–19,607, doi:10.1029/95JA01755.

Weimer, D. R., L. A. Reinleitner, J. R. Kan, and I. S.-Akasofu (1990), Saturation of the auroral electrojet current and the polar cap potential, *J. Geophys. Res.*, *95*, 18,981–18,987, doi:10.1029/JA095iA11p18981.

Winglee, R. M., D. Chua, M. Brittnacher, and G. K. Parks (2002), Global impact of ionospheric outflows on the dynamics of the magnetosphere and cross-polar cap potential, *J. Geophys. Res.*, *107*(A9), 1237, doi:10.1029/2001JA000214.

Wygant, J. R., R. B. Torbert, and F. S. Mozer (1983), Comparison of S3–3 polar cap potential drops with the interplanetary magnetic field and models of magnetopause reconnection, *J. Geophys. Res.*, *88*, 5727–5735, doi:10.1029/JA088iA07p05727.

Yan, M., L. C. Lee, and E. R. Priest (1992), Fast magnetic reconnection with small shock angles, *J. Geophys. Res.*, *97*, 8277–8293, doi:10.1029/92JA00170.

J. E. Borovsky, Los Alamos National Laboratory, Mail Stop D466, Los Alamos, NM 87545, USA. (jborovsky@lanl.gov)

M. M. Kuznetsova, NASA Goddard Space Flight Center, Code 674, Greenbelt, MD 20771, USA.

B. Lavraud, Centre d'Etude Spatiale des Rayonnements, UMR5187, CNRS, F-31028 Toulouse, France.